A Cryogenic Buffer Gas Beam of Ytterbium Atoms

Danny George

Masterarbeit in Physik
angefertigt im Institut für Angewandte Physik

vorgelegt der
Mathematisch-Naturwissenschaftlichen Fakultät
der
Rheinischen Friedrich-Wilhelms-Universität
Bonn

December 2025

I hereby declare that this thesis was formulated by myself and that no sources or tools other than those cited were used.

Bonn, 01-12-2025 .....
Date

.....
Signature

1. Gutachter: Prof. Dr. Daqing Wang
2. Gutachter: Prof. Dr. Sebastian Hofferberth

Contents

Acknowledgements

I would like to express my gratitude to Prof. Dr. Daqing Wang for the opportunity of working on this project. I would also like to thank the entire Nanophysics and Quantum Photonics group for welcoming me into their team. I am also grateful to Prof. Dr. Sebastian Hofferberth for taking his time to be the second examiner for this thesis. I would like to thank my lab partners Nick, Yumi, Lucas, Simon and Jan for their continued support and knowledge that was required for making this project and thesis possible. I would especially like to express my gratitude to Nick for taking his time to teach me all the ins and outs of vacuum systems and all the engineering and design knowledge that I lacked over the last twelve months. I would like to thank Max, Fang, Babak, Ricardo and Bo for taking their time to answer all my questions, without hesitation, helping me brainstorm solutions to different problems that were encountered during the last year. I would like to especially thank Hazem, Delia and Kathrin for their support and discussions. I would also like to thank Mr. Graf and the entire workshop team for all the parts and prototypes required for making the machine a reality. Finally, I want to express my gratitude to my family in India and my friends in Cologne for their continued support and motivation throughout the master's programme for the last two years.

CHAPTER 1

Introduction

Over the last forty years, researchers have been cooling and trapping atoms using laser light. This was motivated by the desire to make better clocks and more precise spectroscopy. However, it was quickly realised that molecules could also benefit from these cooling methods. However, typical techniques for cooling and trapping atoms cannot be easily translated to molecules, and they were considered to be extremely difficult to implement. Cold molecules offer possibilities for precision tests of fundamental physics, such as estimating the electron dipole moment [1], as well as multitudes of quantum technologies [2] along with studies into molecular collisions [3]. There are many methods of slowing molecular beams down from deceleration from the electric field using the Stark effect or the Zeeman slower, which utilises magnetic fields, or your typical Doppler slowing and trapping schemes. However, all these slowing and trapping methods for molecules require an intense beam to have a better chance of trapping any molecules. And since there is a compromise between the molecules that are decelerated and how much deceleration can be achieved, an intense source of slow-moving molecules is required [4]. An effective way of producing slow-moving cold molecules was first introduced by Maxwell [5] in 2005, which was later developed by Paterson and Doyle [6] and many others. After roughly twenty years of development on these buffer gas sources, they have now become an essential part of the toolkit that is required to tackle cold molecules. There has been significant research into buffer gas sources, as it provides a way of cooling molecules down, especially their internal degree of freedom. All implementations of a typical cooling scheme of atoms can now be applied to molecules, albeit with some modification.

The goal of this thesis was to materialise a buffer gas source for the cold molecule beam, which would enable exciting experimental work looking into fundamental forces of nature as well as a deeper look into quantum technologies. To produce the buffer gas source, multiple iterations were done to explore what works but also implement some insight that we got from recently published exploration of the workings of the buffer gas cell [7]. This requires rapid iteration and modification to the machine at every step. During the course of building the machine and iterating it multiple times, we iron out different processes, making it efficient and less time-consuming.

We will begin by understanding the inherent properties of molecules and which of these properties makes cooling molecules difficult in section (2.1). After that we will delve into different cold molecule sources and understand why buffer gas sources are more suitable for trapping and cooling molecules and discuss the buffer gas source as well in section (2.3). After that, the thesis includes a concise snapshot into the journey required for materialising the source, as well as the complementary measurement section

to finally characterise the beam as seen in chapter (3). However, due to time constraints, as well as the overall ease with which ytterbium can be handled and used, it was decided that instead of fully building the machine for producing molecules, all the key parts for just the production of a cold beam of atoms were given priority. That is why, while there may be some parts that were built for the goal of producing molecules, these will not be discussed in detail. Instead, most of the work will be focused on materialising a cold helium beam with ytterbium in it. While it would be relatively easy to add the final finishing touches for the production of molecules, it was prudent that the behaviour of the helium beam itself was explored. Thus, in chapter (4) the ytterbium beam will be explored and characterised, finally ending with some insights into how the machine works and possible improvements required before producing a molecular beam.

CHAPTER 2

Theory

2.1 Molecular Energy Levels

Molecules, like atoms, have quantised energy levels, but due to the complexity that arises because of the proximity of electrons to multiple nuclei and other electrons, the energy level schemes of molecules become more complex. This could be described by considering the individual atoms as hard spheres. By adding just two atoms, this allows for new degrees of freedom, mainly the rotation of the two atoms, as well as the vibrations that can occur between the two atoms. Thus, it requires the use of different notations to refer to these energy levels.

The total energy of an electron in a molecule can be written as the sum of the energy quantisation from the electronic state of the molecule along with vibrational and rotational motions of the nuclei, with other smaller effects such as spin-orbit coupling and nuclear spin interactions.

$$E_{\text{total}} = E_{\text{electronic}} + E_{\text{vibrational}} + E_{\text{rotational}} + ... \tag{2.1}$$

Each energy quantisation requires a different notation to fully examine a transition [8].

2.1.1 Electronic States

Like atoms, molecules have a set of electronic states, in which each energy level corresponds to a different electronic configuration. These energy levels are typically the largest in energy spacing. The ground state is always labelled X, while the excited states are labelled alphabetically, A, B, C etc., with increasing energy. But each energy level is also a function of the distance between the nuclei R. Thus, each electronic level can be plotted as a function of internuclear spacing $E_e(R)$.

To add more information about the total angular momentum and spin, electronic states are often represented along with term symbols shown in equation (2.2).

$$^{2S+1}\Lambda^{+/-}_{g/u} \tag{2.2}$$

Where S is the total electronic spin quantum number, thus $2S + 1$ giving the spin multiplicity. Λ is the projection of the total angular momentum along the internuclear axis, with values of $\Lambda = 0, 1, 2, 3, \ldots$ corresponding to $\Sigma, \Pi, \Delta, \Phi$. The superscript $+/-$ is used only for Σ states, giving the reflection symmetry

through a plane containing the internuclear axis. The notation g/u is parity with respect to inversion through a centre of symmetry, only applicable to homonuclear molecules. Therefore, a state $X^1\Sigma^+$ refers to a ground electronic state with a singlet symmetry and symmetric with respect to reflection [9].

2.1.2 Vibrational and Rotational States

Within each electronic state, the nucleus executes quantised vibrational motion about its equilibrium position, and these energy levels can be approximated by the harmonic oscillator model along with some corrections.

$$E_v = (v + \frac{1}{2})h\nu_e \tag{2.3}$$

With $v = 0, 1, 2, \ldots$ being the vibrational quantum number and ν_e being the fundamental vibrational frequency. Typical vibrational transitions occur in the infrared region. Also, with each vibrational level, the molecule can also rotate about its centre of mass. From classical mechanics, the energy of a rotating body is $L^2/2I$ with L being the angular momentum and I being the moment of inertia. With quantisation, L^2 is replaced by $\hbar^2 N(N+1)$, where $N = 0, 1, 2, \ldots$ is the rotational quantum number. Thus, the rotational energy levels correspond to:

$$E_r = BN(N+1) \tag{2.4}$$

With $B = \hbar^2/2I$. Thus, a complete molecular state can be described by combining all the quantum numbers:

$$\text{State} : X^1\Sigma^+(v, N) \tag{2.5}$$

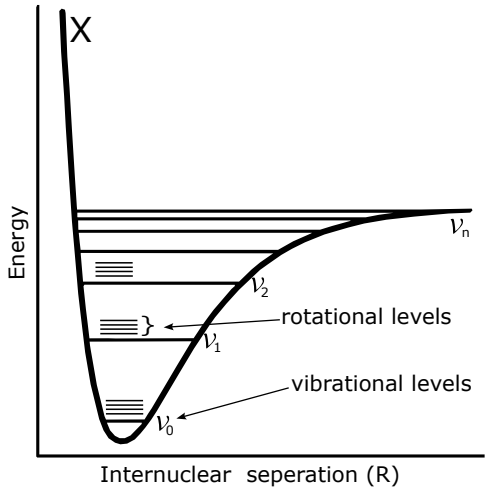

Figure 2.1: Potential energy curves of ground state X as functions of internuclear distance R with vibrational and rotational energy levels shown in the potential.

2.2 Laser Cooling

While there are different methods of cooling under the umbrella of laser cooling, the most common method is via Doppler cooling, and this discussion will be restricted to it as well. The learnings from Doppler cooling can easily be applied to other laser cooling methods as well. An atom has a ground state and an excited state, and the frequency of the transition between these two states is $\omega_\circ$. If the excited state has a lifetime of τ, then the natural linewidth of this transition is $\Gamma = 1/\tau$. Typically, $\Gamma \approx 10^{-8}\omega_\circ$ as atomic resonances have an extremely narrow linewidth. When an atom interacts with a counter-propagating beam of frequency ω with respect to atomic motion, which has a slight shift below the resonance frequency, the beam is said to be 'red-detuned' with $\delta_\circ = \omega - \omega_\circ$ being the detuning. When the Doppler shift of the atom travelling at a velocity $\vec{v}$ is $\delta_D = -\vec{k} \cdot \vec{v}$ matches the detuning, a ground state atom can be excited by absorbing a photon from the laser beam. The momentum of the absorbed beam is taken by the atom, thus reducing its momentum by $\hbar k/m$, with m being the atomic mass. The excited atom can decay spontaneously in a random direction. Thus, this repeated sequence of absorption in one direction and decay in any random direction starts slowing the atom repeats until the atom is in resonance. By tuning the laser frequency, an atom can be slowed down with velocities close to zero. The force experienced during this sequence is called the scattering force.

For an atom interacting with a single laser beam of intensity I, the scattering rate is:

$$R = \frac{\Gamma}{2} \frac{I/I_s}{(1 + I/I_s + 4\delta^2/\Gamma^2)} \tag{2.6}$$

While this simple model of two-state system approximation works for atoms due to their inherent small linewidth and other excited states being far away, it is a different story for molecules.

2.2.1 Why Laser Cooling is Difficult for Molecules?

Typical Doppler cooling of atoms at room temperature requires at least 10^4 scattering events to bring the speed from roughly 300 m/s at room temperature close to zero, which requires a "closed" transition, without the atom decaying to any of the intermediate states that are not resonant with the laser. For molecules with the added complexity of rotational and vibrational states, it is difficult to ensure that the cooling cycle remains "closed". Say, for example, we have a transition being driven from the electronic ground state, X, with vibrational and rotational quantum numbers v and N, which is the ground state labelled $|g\rangle = |X, v, N\rangle$, to an excited state $|e\rangle = |A, v', N'\rangle$. The probability of decaying to the ground state from (v') to any (v'') is

$$P_{v',v''} = \left| \int \Phi_{X,v''}(R)\Phi_{A,v'}(R)dR \right|^2 . \tag{2.7}$$

The above equation is also known as the Franck-Condon Factor, which is the square of the overlap integral between two vibrational wave functions of states A and$X$. If we look into the Frank-Condon factor($P_{v',v''}$) for multitudes of molecules, only a few candidates have $P_{v',v''} \approx 1$ when $v'' = v'$ and closer to zero for all other transitions. This implies that a closed transition is possible in these candidates, with some repump lasers to close out all the branches to close this transition. But if we consider Calcium mono-fluoride (CaF) one of the better candidates for laser cooling, after 2×10^5 photon scattering events,

the molecule leaks out of the cooling cycle. And because of its higher mass, more scattering events are required to effectively slow these molecules down. Therefore, it is quite evident that other methods of cooling these molecules are required, to not just slow and trap these molecules, but also allow laser cooling in the first place, as at room temperature, molecules occupy higher rotational and vibrational energy levels. Hence, we need a cooling method to produce slow beams of cool molecules for laser cooling and other spectroscopic measurements as well.

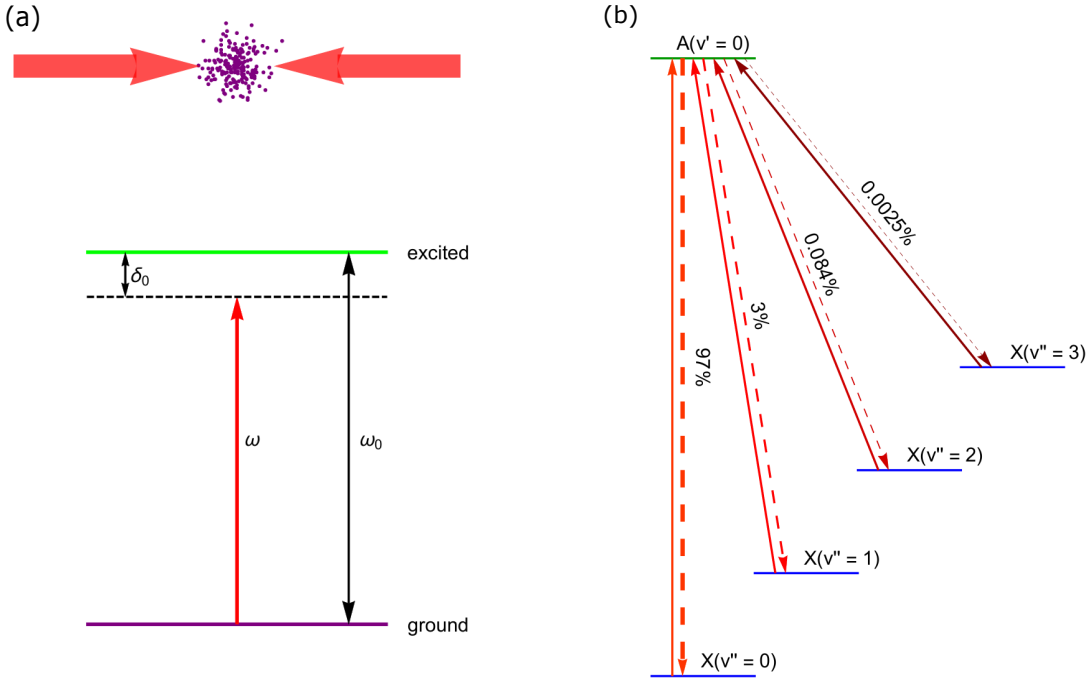

Figure 2.2: (a) One dimensional doppler cooling. (b) CaF sublevel scheme for laser cooling with Frack-Condon factor for each decay [8].

2.3 Cryogenic Buffer Gas Sources

In this section we will be dealing mainly with cryogenic buffer gas cells, a novel method of producing cold and slow beams of atoms and molecules for a multitude of applications, but before we dive into this source, I would like to introduce some key ideas to better understand the workings of this source.

2.3.1 Cold Molecule Sources

There are mainly two kinds of cold molecule sources, supersonic expansion sources and cryogenic buffer gas sources, where both use a carrier gas into which the target atom or molecule to be cooled is introduced. Thus, the gas should be inert so that it does not react with the target. The cooling mechanism of the beam, however, is different. While supersonic sources rely on the adiabatic expansion of their carrier gas into a vacuum as their cooling mechanism, cryogenic buffer gas sources use external cooling methods to ensure that the carrier gas is cooled. To facilitate adiabatic expansion from a nozzle as shown

in figure (2.3), a high pressure difference between the vacuum side and the chamber is required. However, due to this expansion, the subsequent beam that is formed has a high forward velocity, around 600 m/s. This makes supersonic sources a bad candidate for cold molecule experiments where high interaction times and/or trapping are involved. Cryogenic sources work in much lower forward velocity regimes, typically around 150 m/s, enabling experiments and measurements involving high interaction times as well as optical slowing and trapping mechanisms.

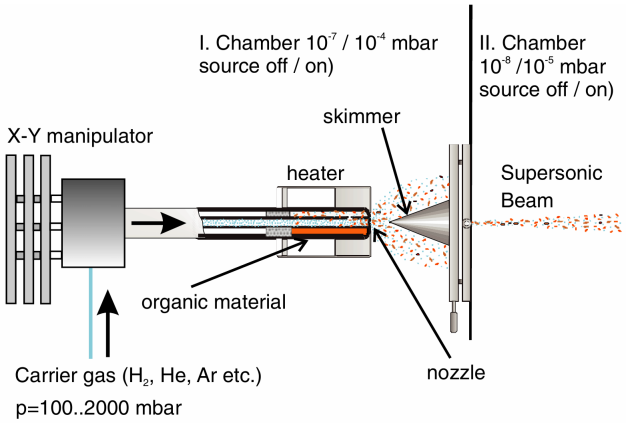

Figure 2.3: A typical supersonic source [10].

2.3.2 Flow Regimes

To characterise gas flow regimes of different sources, the Reynolds number can be used, in particular at the source exit which produces the beam. The Reynolds number is defined as the ratio of the viscous and inertial forces in a fluid flow.

$$Re = \frac{F_{\text{inertial}}}{F_{\text{viscous}}} = \frac{\rho v^2 d^2}{\mu v d} = \frac{\rho v d}{\nu} \tag{2.8}$$

Where ρ is the density, v is the flow velocity, μ is the dynamic coefficient of viscosity and d is the characteristic length, which in this case would be the exit aperture diameter. The Reynolds number can also be related to kinetic quantities, such as the Knudsen number and the Mach number. The Knudsen number is the ratio of the mean free path and d, i.e., $Kn = \lambda/d$, and the Mach number is the ratio of the beam velocity v to the speed of sound in a gas (v_c), i.e., $Ma = v/v_c$. These quantities are related by the von Kaŕmań relation.

$$Ma \approx \frac{1}{2} KnRe \approx 1 \tag{2.9}$$

As the Mach number at the aperture is ≈ 1, which means, $Re \approx 2Kn^{-1} = 2d/\lambda$ referring to the number of collisions at the aperture.

With the Reynolds number at the exit aperture, three different gas flow regimes can be interpreted.

- **Effusive regime**, $Re \lesssim 1$: Almost no collisions are expected, which implies that no significant transformation of the beam occurs while exiting the cell, and it can be assumed to be a simple thermal sampling of the source.

- **Partially Hydrodynamic regime**, $1 \lesssim Re \lesssim 100$: Some collisions are expected near the aperture, changing the beam properties, but not enough collisions to be considered 'fluid-like'.
- **Fully Hydrodynamic regime**, $100 \lesssim Re$: The carrier gas behaves like a fluid due to a large number of collisions, leading to adiabatic expansion.

Supersonic beams are in the fully hydrodynamic regime, while buffer gas source beams operate in the partially hydrodynamic regime [11].

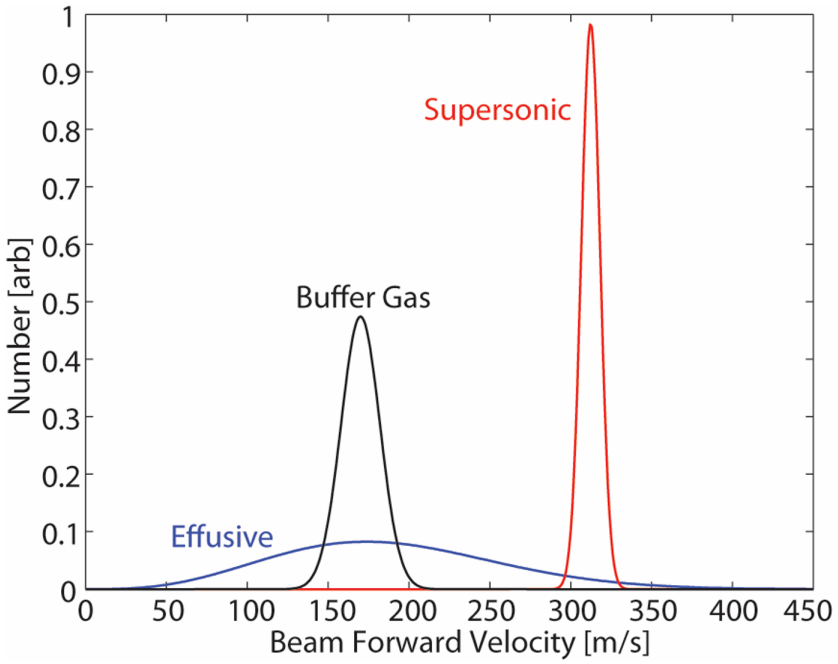

Figure 2.4: Velocity distribution for different cold molecule sources, in different flow regimes [11].

We can also identify the different regimes by comparing their velocity distribution, as shown in figure (2.4). In near-effusive regimes we do not expect the typical Maxwell-Boltzmann velocity distribution for a fully thermalised gas source. Instead, for beams in near-effusive regimes with small amounts of hydrodynamic effects, the velocity distribution is given by:

$$p_{\text{eff}}(v) = Av^3 \exp\left(\frac{m^* v^2}{2k_B T}\right) \tag{2.10}$$

with m^* being the effective mass of the beam and T being the temperature of the source itself and not the beam. The velocity distribution for supersonic beams, that is a beam in fully hydrodynamic regime is given by:

$$p_{\text{sup}}(v) = Av^3 \exp\left(\frac{M(v - v_0)^2}{2k_B T_{\text{beam}}}\right) \tag{2.11}$$

with M being the Mass of the target atom/molecule and v_0 the forward mean velocity of the beam and

T_{beam} the beam temperature [12].

2.3.3 Cryogenic Buffer Gas Cells

As discussed in the previous section, we need a source of cold molecules with a relatively small forward velocity, which ensures that the interaction time of the molecules remains relatively high while also being cooled down to a low temperature to allow access to transitions, enabling laser cooling and trapping, as well as precise spectroscopy, as it decreases frequency broadening from multiple sources as well. A cryogenic buffer gas cell satisfies this condition, which is an enclosed volume which is cooled down to around 4 K, using cryogenic systems. An inert gas is also cooled down to similar temperatures by the cryogenic system, called the buffer gas. The target molecule to be cooled is introduced into the cell itself along with the cooled buffer gas as well. The buffer gas and the target molecule undergo collisions with each other as well as the walls of the cell. This causes the hot target molecules to lose energy to the buffer gas and the cell walls, cooling them down, if enough collisions occur. To ensure this, the dimensions of the cell are chosen to ensure that at least a few collisions occur at a relatively low number density for the buffer gas. After that, the mixture of buffer gas and the target molecule exits the cell through a small orifice into an environment with lower pressure. This produces a beam with a relatively small forward velocity if the gas density inside the cell is low enough to ensure that it is in a partially hydrodynamic regime. The molecule inside the cell can either be introduced directly via a hot needle or via ablation. For ablation, either the molecule itself is ablated, or if diatomic molecules are to be formed, the metal and a reacting gas can also be introduced into the cell so that the molecule itself is produced via a chemical reaction inside the cell [11].

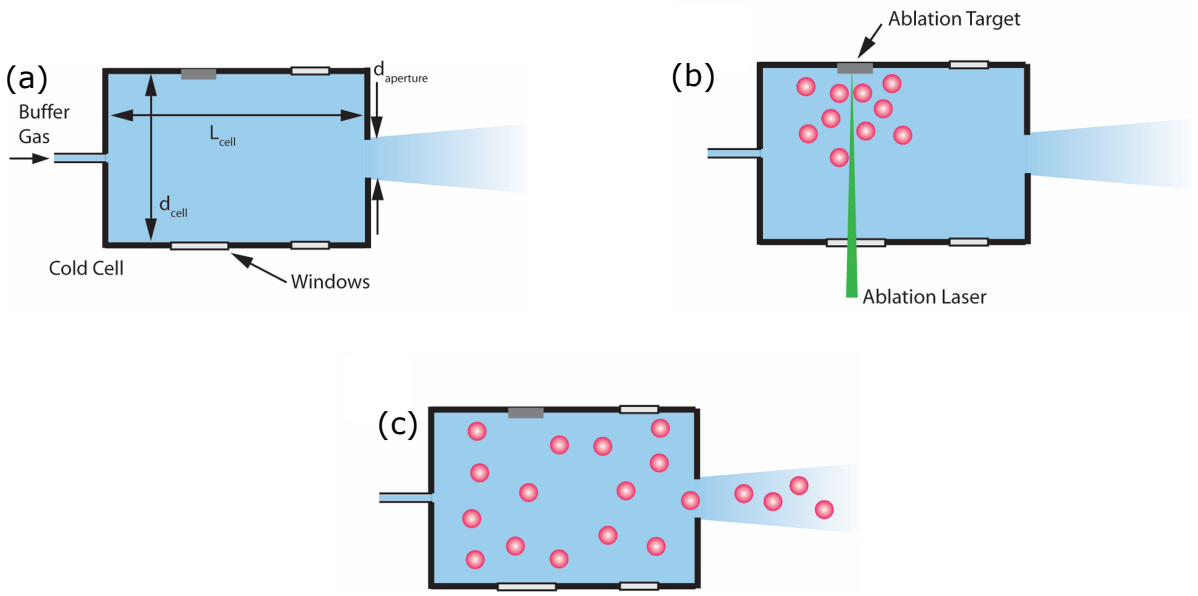

Figure 2.5: A simplified schematic of a buffer gas beam cell. (a) The buffer gas enters the cell through a fill line and exits via a cell aperture on the other side of the cell. (b) Introduction of species via laser ablation. (c) The species thermalises to the buffer gas and forms a molecular beam with the flowing buffer gas [11].

CHAPTER 3

Design and Construction

This chapter explains the design principles for each part of the machine as well as their desired performance metrics. While building the machine, we went through multiple iterations; however, only the final version will be discussed in detail, while mentioning some lessons from the failed attempts.

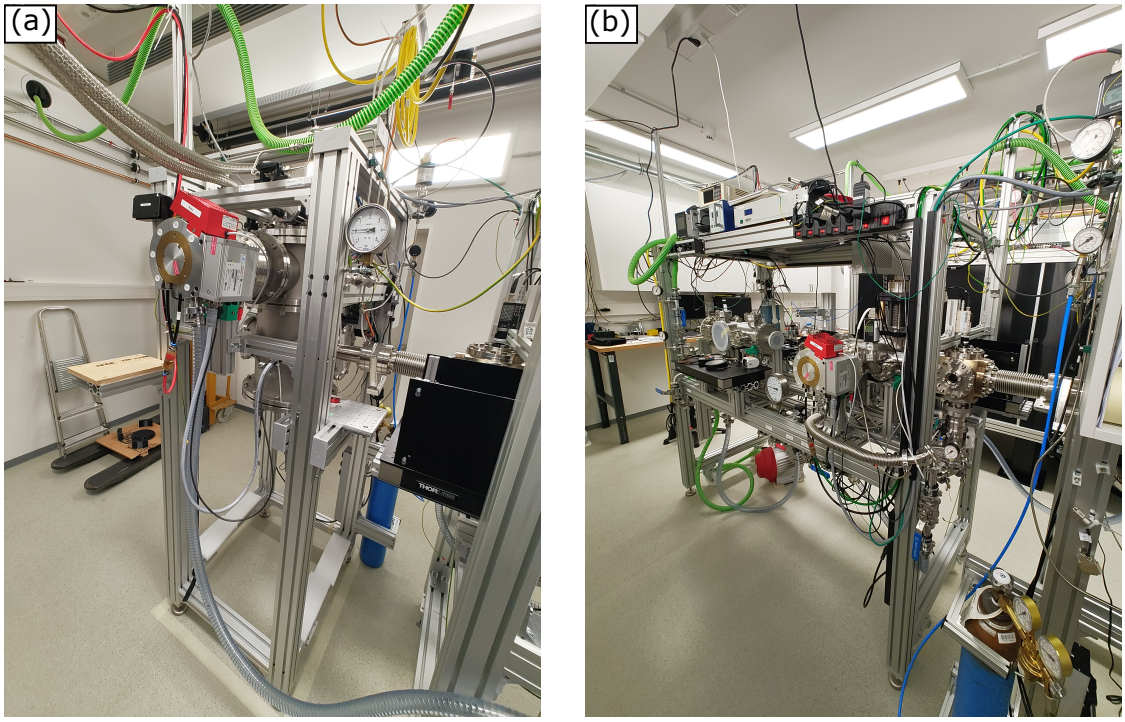

Figure 3.1: Fully constructed machine (a) Source machine and (b) Measurement table.

3.1 Cold Molecule Beam Machine

The cold molecule beam machine produces the the cold buffer gas beam of helium with ytterbium in it. This section or part of the machine will be referred as the source machine or the source chamber. At the heart of the source machine is a cryocooler and its accompanying vacuum enclosure. The vacuum chamber in which the cryocooler is placed is mounted onto extruded aluminium profiles which stand on height-adjustable feet to ensure that the device is always level. Along with the feet, wheels are also mounted to ensure that the source machine can be easily moved and aligned as well, as shown in figure (3.3(b)). The aluminium profile frame allows all the supporting hardware and gauges to be mounted onto the chamber, allowing a flexible design which allows for rapid iteration and modification should they be required.

3.1.1 Two stage Gifford-McMahon Cryocooler

For this setup we are using a 4K cold head 'RDE-418D4' from Sumitomo Heavy Industries Ltd. along with an 'F-50H' compressor unit as well. The Cold Head is a two-stage Gifford-McMahon cryocooler which has a cooling range of 25 K to 50 K for the first stage and a cooling range of 3.5 K to 4.2 K for the second stage. The cooling performance depends on the heat load on each stage. The above-mentioned model has a maximum heat load capacity of 42 W at the first stage and 1.8 W at the second stage. The CAD design of the cryocooler is shown in figure (3.2(a)), with both cooling stages, and the cryocooler mounted on the vacuum housing is shown in figure (3.2(b)).

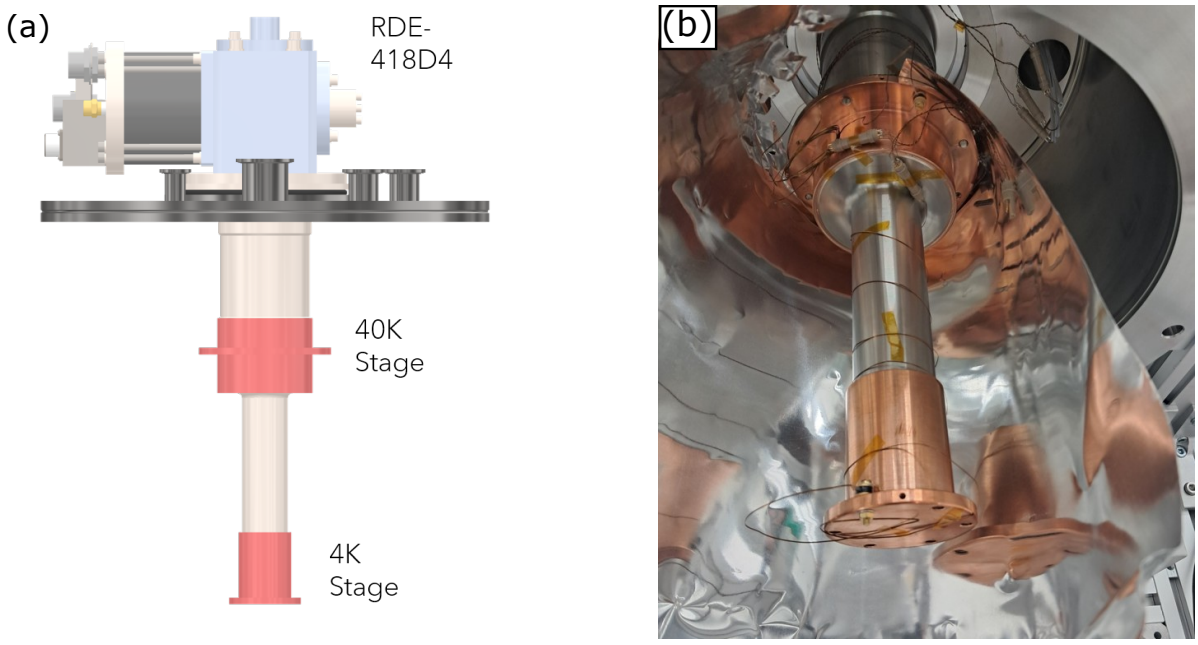

Figure 3.2: (a) CAD design of RDE-418D4 with labels for the two stages [13]. (b) Image of cryocooler mounted in the chamber.

With the help of the two stages of the cryocooler, we are capable of mounting two cooling baseplates, which will be called the 40-K and 4-K stages for easier description. These stages host the cooling coils for the gas lines and the buffer gas cell along with sorption pumps, which, with the help of the cryocooler, will also be cooled to the design temperatures of the cryocooler.

3.1.2 Vacuum System

While producing any kind of beam, an environment with low scattering potential for the beam is always preferable. To achieve such an environment, the cryocooler with its two stages is encapsulated in a cylindrical vacuum chamber with multitudes of ports, allowing for a flexible configuration for feed-through and vacuum pumps. We have a turbomolecular pump (turbo pump) 'HiPace 700' from Pfeiffer Vacuum solutions, attached to the chamber, capable of achieving pressures up to 10^{-8} mbar under ideal conditions.

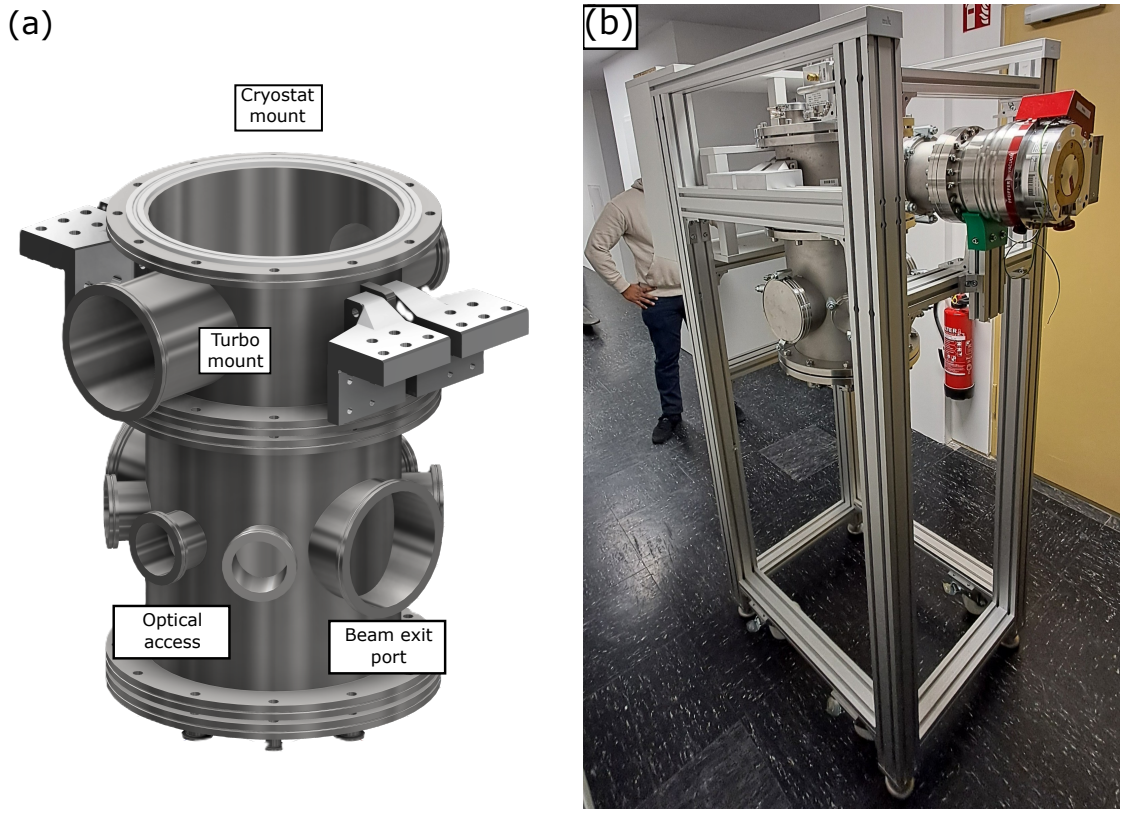

Figure 3.3: (a) CAD design the vacuum chamber: designed by Nick Vogeley. (b) The chamber along with the cryocooler mounted on aluminium frame.

The vacuum chamber is mounted on a frame constructed from extruded aluminium profiles, which allows us to mount all the supporting peripheral systems for controlling and monitoring the source chamber, as shown in figure (3.3(b)). The upper stage of the chamber hosts the turbo pump, and the

second stage allows for the beam to pass onto the measurement chamber with multiple ports for easy optical access within the chamber, as shown in figure(3.3(a)).

3.1.3 Peripheral Systems

Along with the main vacuum chamber and the cold head, multiple other systems, such as a temperature monitoring and gas management system, are also mounted on the frame. The gas management system will be discussed in section (3.6).

For temperature monitoring, we are using Lake Shore Cryotonics' 'Model 218' Temperature Monitor, which is capable of monitoring and transmitting data from up to 8 inputs, shown in figure (3.4(a)). Along with model 218, for temperature measurement, we are using Silicon Diodes (Model: DT-670), also from Lake Shore Cryotonics, which is capable of measuring temperatures in the range of 1.4 K to 500 K. Along with temperature monitoring, vacuum gauges are also mounted to the chamber to monitor pressure within the chamber during the operation of the source machine. For this, vacuum transducers from Thyracont Vacuum Instruments model 'VSM' are used, which are capable of detecting pressure in the range 1000 mbar to 5×10^{-9} mbar, as shown in figure (3.4(b)). With this, we are capable of measuring temperatures in different sections of the cryocooler and monitoring its performance as well as the overall pressure in the chamber.

Figure 3.4: (a) Temperature Monitoring system from Lakeshore Cryotonics [14]. (b) Vacuum gauges from Thyracont Vacuum Industries [15].

3.2 Baseplates and Radiation Shields

At each stage, two baseplates are designed with gas line feedthroughs and threaded through holes so that the radiation shields and heat exchangers can be mounted on these baseplates. They are made out of thermally conducting material, with aluminium being used for the 40-K stage, shown in figure (3.5(a)), and copper for the 4-K stage, shown in figure (3.5(b)). These stages also have G1/4 threaded holes so that parts of the internal gas lines can also be mounted on the baseplate itself.

To achieve the temperatures we target, radiation shields are required. In particular, we need to protect the internal structures of each stage from infrared radiation that will be produced by both the vacuum chamber that surrounds the cold head and visible radiation from the multitude of windows that are also

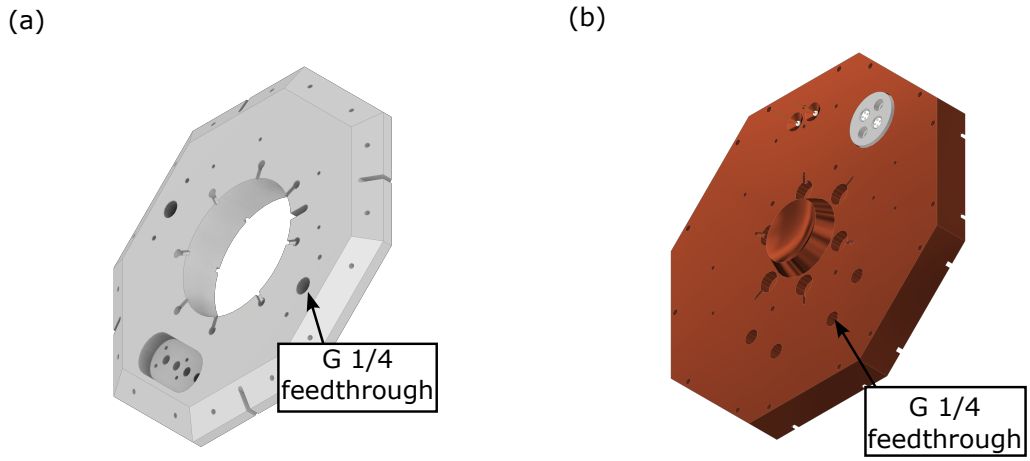

Figure 3.5: (a) 40-K (b) 4-K baseplates mounted directly to the cryocooler.

mounted on the chamber. By blocking the line of sight between the external surfaces and the internal structures of the cooling stages, we could block all heating sources via visible radiation. But if the shields themselves remain at room temperature, they will again act as a source of infrared radiation. Therefore, we mount two sets of radiation shields, one on each stage, both made out of copper, so that the shields themselves are also cooled to the temperature of each cooling stage protecting the internal surfaces from the infrared radiation. Each stage has its own radiation shielding, but have different roles.

3.2.1 40-K Radiation Shield

The 40-K radiation shield is mainly used to protect the internal structures from infrared radiation, and without it the second stage would not reach temperatures below 4 K. It is constructed out of copper sheets 1 mm in thickness. These shields are mounted onto the 40-K stage using setscrews, which are screwed onto the stage, with the shields hung on them. After that, the shields are secured using washers and nuts. The bottom of the shield is constructed out of aluminium and is a regular octagon with a thickness of 5 mm. It also includes some M3 threaded holes so that temperature sensors can be mounted on the bottom as well. There are also access holes drilled on the radiation shield to allow for optical access as well as a hole for the beam to pass through, as shown in figures (3.6(a)) and (3.6(b)).

3.2.2 4-K Radiation Shield

The 4-K shields also provide protection from infrared radiation and function just like the 40-K shields. But these shields also have another important role, where they host the sorption pumps made out of coconut charcoal. Sorption pumps allow for the pumping of helium from the cell onto the surface of the charcoal when shields themselves are cooled to roughly around 4 K. The radiation shields are designed such that they could be mounted to the 4-K stage baseplate using some through holes. These are also made out of copper, but since they also host the sorption pumps, they are CNC machined

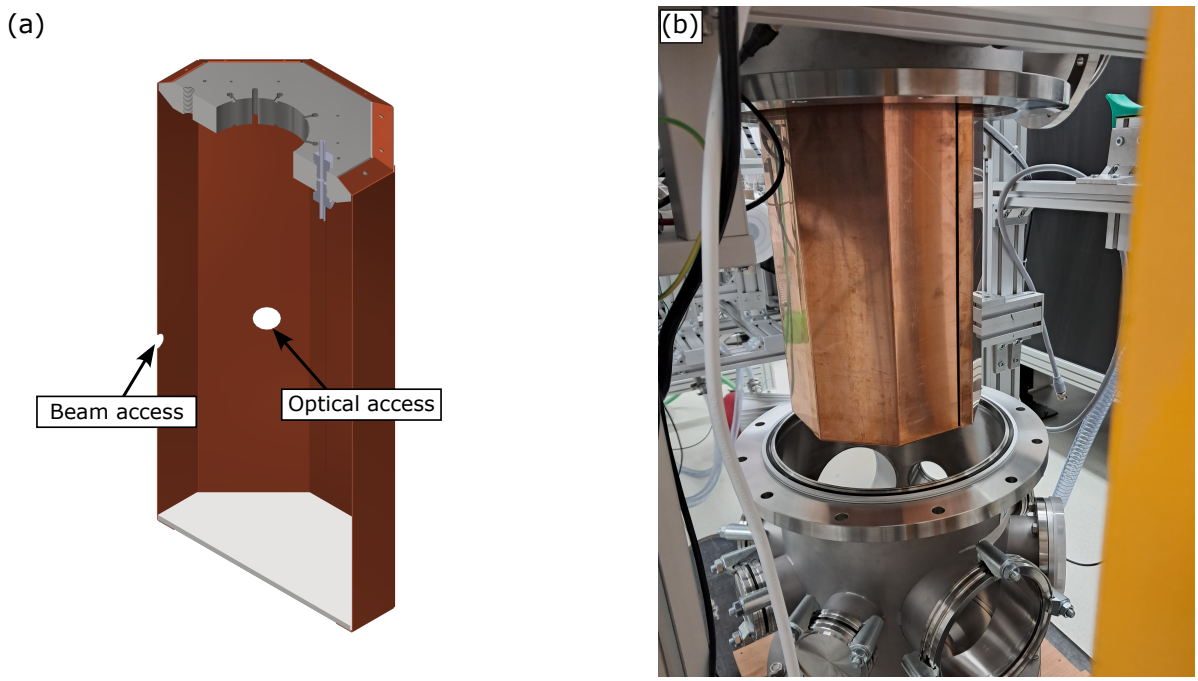

Figure 3.6: (a) Half-section view of 40-K radiation shield CAD design. (b) 40-K shield plates mounted to its baseplate.

from solid copper, as shown in figure (3.7(a)). The shield mainly consists of 8 walls and an octagonal cover plate, and all the internal surfaces are coated with charcoal. The walls of the shield have a small lip at the top and bottom to ensure that the charcoal, along with the glue used to stick it to the walls, is constrained as well, as shown in figures (3.8(a)), (3.8(b)) and (3.8(c)). As with the 40-K shields, there are also holes made to ensure that there is optical access to the cell and also smaller holes for the beam as well. The two optical access holes can also be closed using their appropriate plugs so that the internal systems are not heated up unnecessarily if that particular optical access is not being used.

The glue used for the purpose of sticking charcoal to the walls and base should also be vacuum compatible, which means that it should not outgas when in a vacuum. The glue used for this purpose is the 'LOCTITE STYCAST 2850KT' and 'CAT 24LV', which is a resin-based glue along with a hardener. The glue requires curing to properly harden and ensures that it doesn't outgas in a vacuum. The two-part resin glue is first prepared and coated on top of the internal surfaces of the radiation shield. After that, charcoal is sprinkled on top of the still wet glue so that it gets stuck to it. Then the charcoal and glue are cured for multiple hours at varying temperatures to ensure that they are fully hardened, as shown in figure (3.8(a)).

3.3 Buffer Gas Cell

To produce a cold molecule beam, a buffer gas cell is required. In a buffer gas cell, the atoms or molecules of our interest are introduced into a partially closed cell along with a cooled inert gas, usually helium or

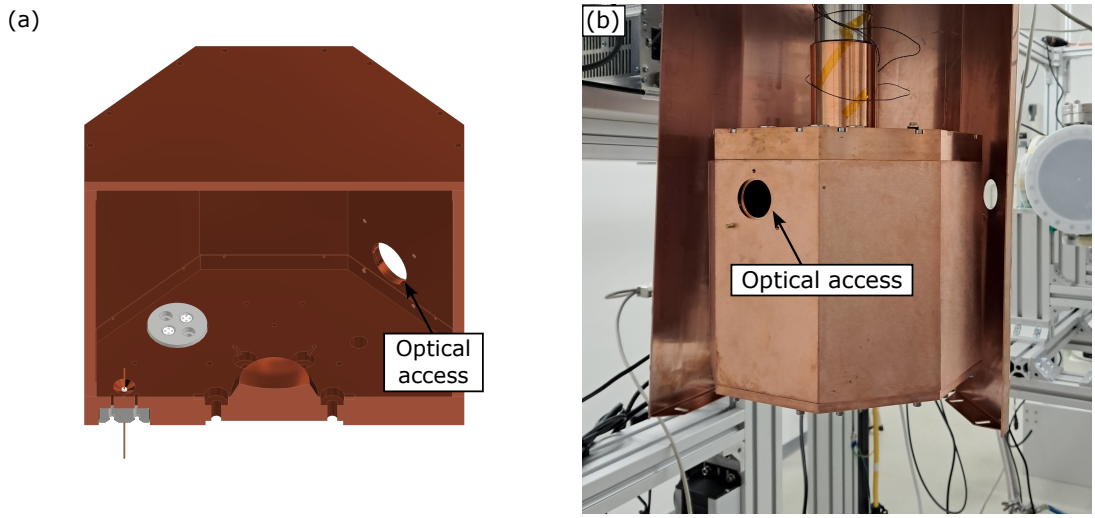

Figure 3.7: (a) Half-section view of 4-K radiation shield CAD design. (b) 4-K shield plates mounted to its baseplate.

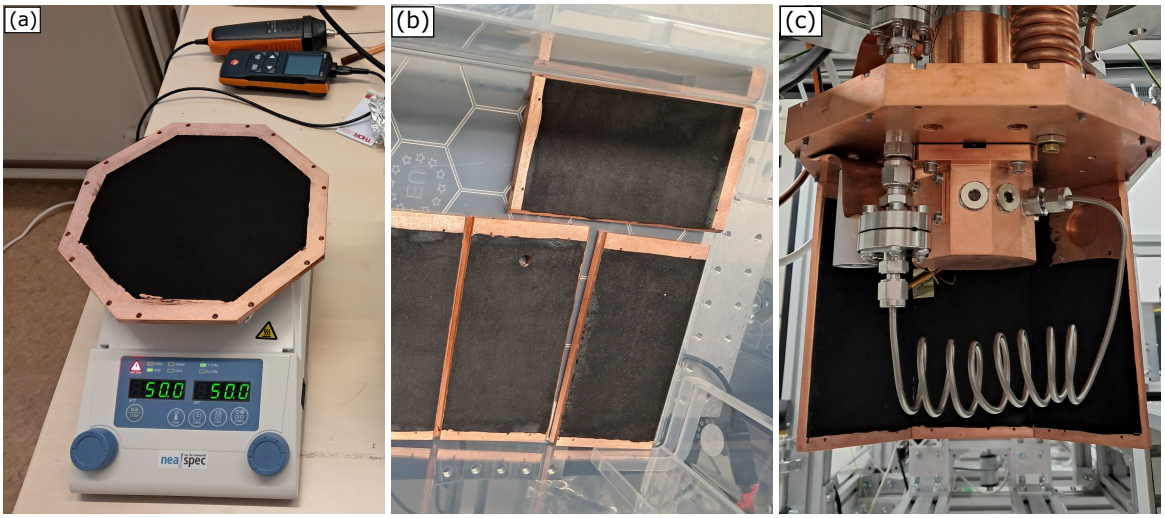

Figure 3.8: (a) Cover plate being cured with charcoal. (b) Fully cured walls of the 4-K radiation shield. (c) Partially mounted 4-K radiation shield.

neon, called the buffer gas. This helps to thermalise the particles of interest. After that, the mixture of the buffer gas and the target atom/molecule exits through a small orifice, thus producing a beam. While inside the cell, the target species being cooled undergoes a number of collisions with the buffer gas, allowing for translational and rotational temperatures to be cooled. The yield of the target species depends heavily on the density of the helium inside the cell and the cell geometry. We are restricted by the pumping capacity of our sorption and turbo pumps (controlling the vacuum level outside the cell orifice) to have any meaningful control of the helium density inside the cell. We can fine-tune the geometry of the cell to ensure a maximum throughput for the target species. As such, we want to design

a cell allowing for some sort of flexibility in the geometry of the cell. Thus, a particular design was finalised after iterations and changes, which allows us to change different parameters of the cell.

- Orifice diameter and its shape.
- Injection angle of the helium with respect to the axis of the orifice.
- Introduction of the target species into the cell.

The external shape of the cell is not at all fixed by any of the parameters but comes naturally from the internal shape of the cell after ensuring that all the different modules for the cell could be mounted. The design was finalised on an irregular nine-sided external shape as shown in figure (3.9). Along with the mounting base, the typical cell dimensions are $(80 \times 64.5 \times 53)$ mm.

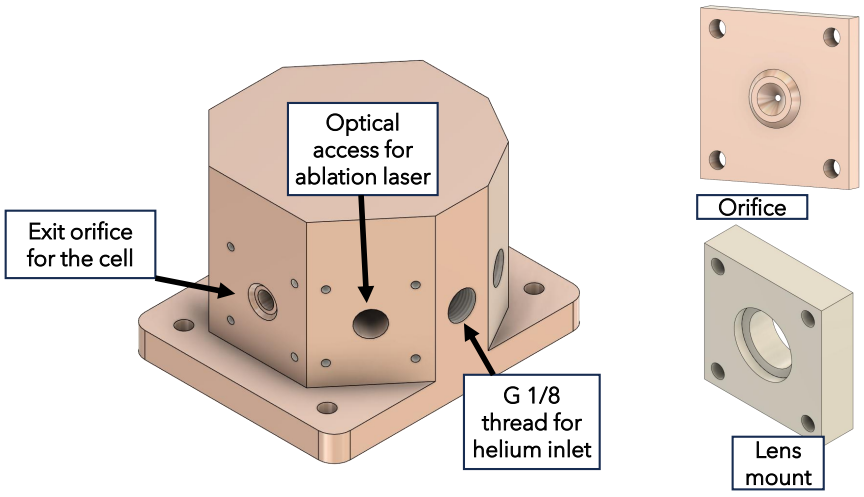

Figure 3.9: Buffer gas cell CAD design with two examples of mountable pieces, a lens mount and the orifice.

Internally, the cell has a cylindrical cavity capped by a hemisphere of diameter 35 mm which ends in a conical sealing surface as shown in figure (3.10(a)). Along the internal cylinder there are multitudes of ports for access into the cell interior, with two main 8 mm diameter holes and one 5 mm diameter hole. The rest of the ports are G1/8 threaded holes allowing for multitudes of connections into the cell, which will be used for adding helium inlets to the cell at varying angles. All the G1/8 threaded ports can be used for helium and, down the line, SF_6 so that we could produce a molecule as well. Along with the main cell, a lot of complementary pieces were also designed to allow testing of its sealing capacity and other parameters of the cell, also shown in figure (3.9). It includes plugs for both 8mm and 5mm holes as well as a lens mount and an oven mount to allow us to change ways of introducing atoms into the cell.

The different ports for mounting the helium line onto the cell were designed so that the angle at which helium is introduced into the cell can be changed. This was done partially with inspiration from my colleague Nick Vogeley's recent paper [7], which explored the beam flux with respect to injection angle numerically, and it will be tested in this setup in the near future. Other parameters of the cell can also be changed, using the different mountable pieces. For example the diameter of the exit orifice can be changed by make a new orifice piece, instead of making changes to the cell itself. The way of introducing

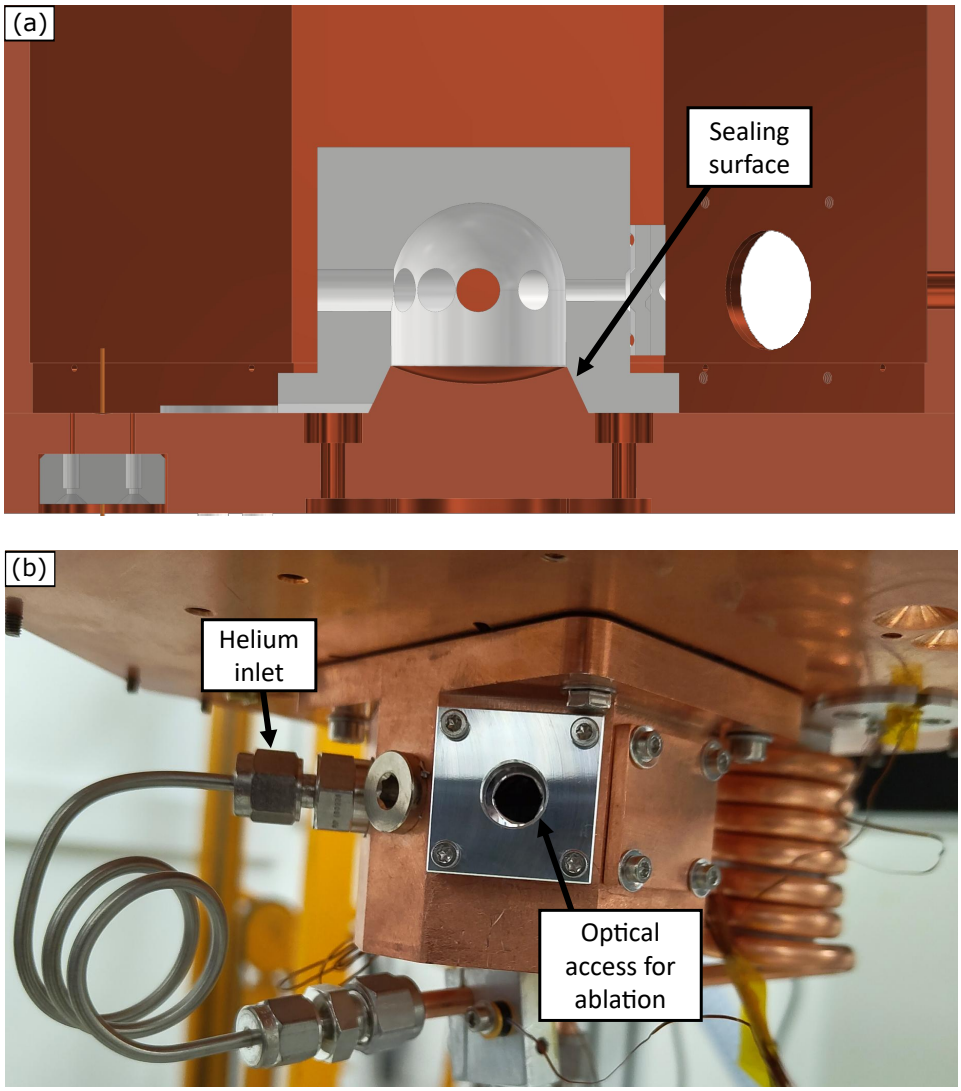

Figure 3.10: (a) Half-section view for the cell and the base plate. (b) Image of the cell mounted on the base plate of the 4-K stage.

ytterbium atoms into the cell can also be changed with either laser ablation or a hot oven. Thus different parts for the ability to do both were designed and manufactured. However it was decided that laser ablation will be used for producing ytterbium vapour inside the cell. The reasons against using an oven for ytterbium are mentioned in section (6).

3.4 Measurement Table

The measurement table holds a secondary chamber called the measurement chamber, which hosts the Quadrupole Mass Spectrometer (QMS) and a CF100 cube to allow for the characterisation of the beam via mass spectroscopy with the QMS and fluorescence spectroscopy using the windows mounted on

the CF100 cube. The quadrupole mass spectrometer uses a quadrupole to filter masses by altering the voltage across it and only allowing ionised particles satisfying a particular mass-to-charge ratio and detecting those particles. We are using the 'HAL RC PIC-RGA 511' QMS from Hiden Analytical. At the bottom of the measurement table, the Pre-Vacuum lines are mounted, which will be discussed in section (3.7). The secondary chamber is connected to the source chamber with a bellow and a gate valve to allow separation of the two chambers so that one chamber can be opened while preserving the vacuum in the other chamber. To the measurement chamber, another two turbo molecular pumps are mounted to ensure that the pressure in the secondary chamber stays low, as the QMS can only be operated safely if the pressure is below 6.6×10^{-6} mbar. This is shown in figure (3.11(b)). There is also a CF100 cube just before the measurement chamber where the QMS sits to allow for optical access to the beam, allowing for Doppler-free characterisation of the beam. It hosts a multitude of zero-length reducers to mount CF40 windows to which Thorlabs cage systems can be fixed, enabling optics to be mounted directly to the cube without the use of breadboards. Here is also where the secondary turbomolecular pump is also mounted, shown in figure(3.11(a)), allowing for even better vacuum in the whole measurement chamber.

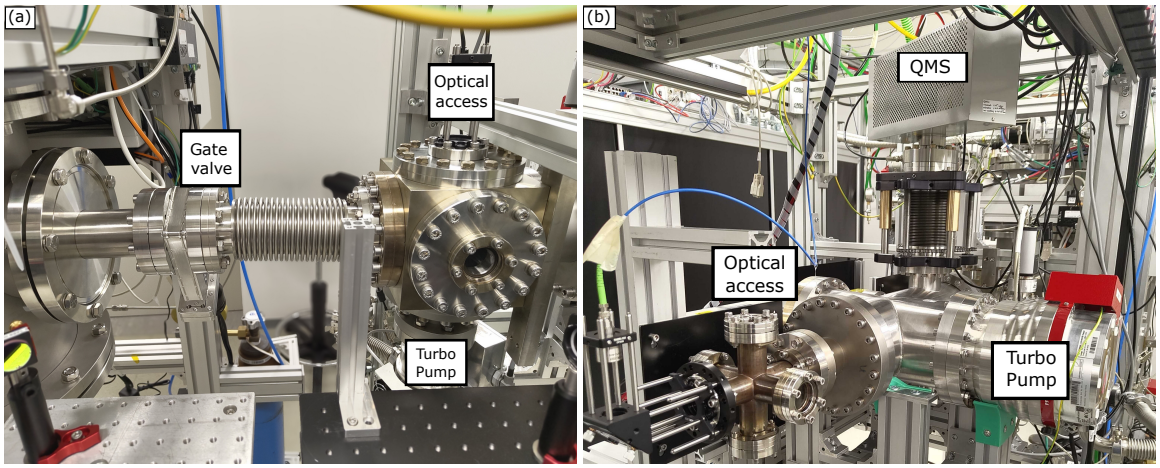

Figure 3.11: (a) The CF100 cube hosts a turbo pump along with the bellow and the gate valve connecting to the source chamber. (b) Measurement chamber with all major parts annotated.

There is also optical access along the beam path to allow for a Doppler measurement as well, shown in figure (3.11(b)). Because of the bellow that connects the two chambers being a bottleneck, the pressure within the measurement chamber remains typically one order of magnitude lower. This is essential to allow the safe operation of the QMS as well as keep the beam from dispersing due to collision with other particles within the vacuum chamber.

3.5 Production of Atoms

Alongside the measurement chamber sits the Ablation Laser, a 532 nm pulsed laser with a pulse duration of 10 ns from CNI Lasers 'LPS-532-A-100mJ-GC30536', which sits on a raised breadboard, ensuring

that the laser head height is the same as that of the cold beam height, shown in figure (3.12(b)). It goes through a series of mirrors before entering the chamber through a window. The beam is steered into the chamber via optics sitting on a separate breadboard, mounted on the frame, hosting the source chamber, as shown in figure (3.12(a)). With cut-outs made in the radiation shield of both the 40-K and 4-K stages, the beam is focused onto a target filled with ytterbium, shown in figure (3.12(c)), allowing the production of a hot vapour of ytterbium atoms within the buffer gas cell.

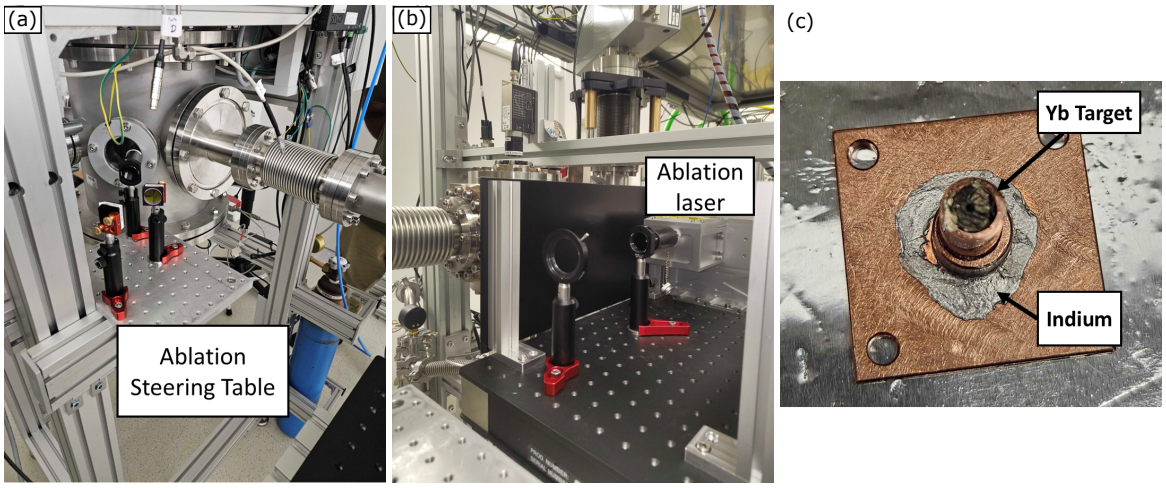

Figure 3.12: (a) Breadboard fixed to the source chamber's frame for steering the laser into the cell. (b) Ablation laser placed on top of a raised breadboard to match the cell's height. (c) Ablation target fixed onto the cell, filled with ytterbium.

3.6 Gas Management System

In this section we will be discussing the auxiliary system for introducing mainly He into the chamber, cooled to roughly 4 K and then finally into the buffer gas cell to enable the production of a cold molecule beam. The gas management system can broadly be divided into two subsystems.

- External pressure and flow management.
- Internal temperature management.

While some portions of the external gas lines were also built for the planned molecular side of the experiment, providing SF_6 to the buffer gas cell, the internal gas line was only built for helium.

3.6.1 External Pressure and Flow Management

This section of the gas lines manages to reduce the pressure from a 200 bar He gas bottle to roughly 2 bar for helium and from 12 bar to 1 bar for SF_6 with the help of multitudes of pressure reducers, shown

in figure (3.13(b)), and at each reduction the pressure is monitored as well. All the gas lines are made out of 6 mm outer diameter 316 stainless steel tubing, and the connections to 90° bends and T pieces are done with the help of Swagelok connectors. These finally connect through long coils of tubing to the Mass Flow Controller, as shown in figure (3.13(d)), so that we could finely control the flow of each gas into the chamber. The mass flow controller measures and controls the flow of gas by measuring the heat loss due to gas flow. It measures in units of standard cubic centimetre per minute (sccm).

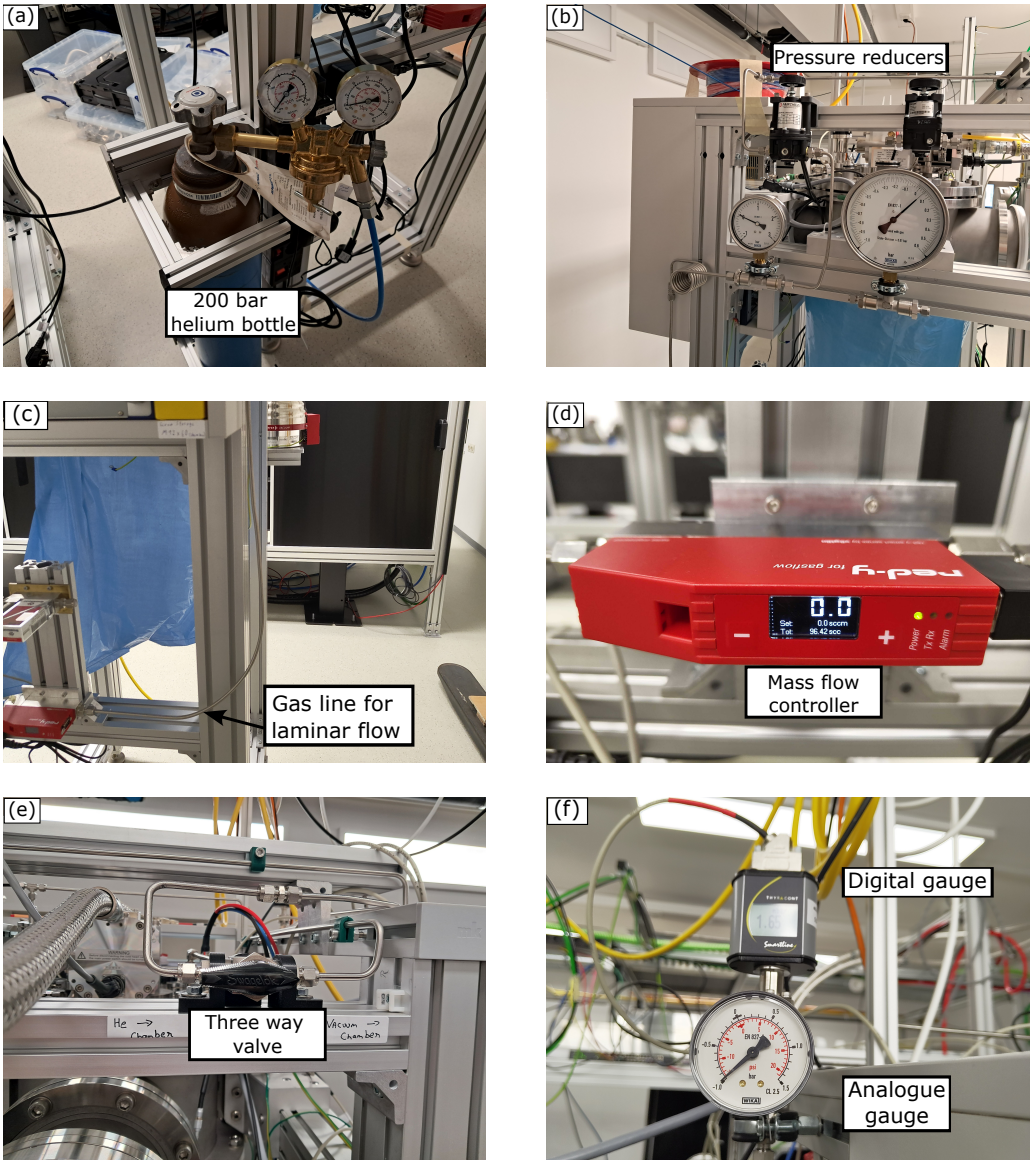

Figure 3.13: (a) 200 bar helium gas bottle with a pressure reduction to 20 bar. (b) Pressure reducers for both helium and SF_6 with their manometers. (c) a straight section of tubing for laminar flow of helium to the mass flow controller. (d) Mass flow controller to measure and check the flow of helium in sccm. (e) 3-way valve to either allow helium to flow into the chamber or evacuate the gas lines by connecting to the source chamber directly. (f) Combination of digital and analogue gauges connected to a CF 16 cross.

The typical gas flow that will be used during the operation will be between 1 sccm and 10 sccm. For accurate measurement by the mass flow controllers, a laminar flow is required. Thus, the tube before and after the mass flow controller has shallow bends and long straight sections, shown in figure (3.13(c)). These finally get connected into a three-way valve so that the system can either be connected to the internal gas line or be connected to the vacuum chamber so that the gas lines themselves can be evacuated as well, as shown in figure (3.13(e)). There is also a digital pressure gauge to record the pressure in this section of the gas line along with an analogue gauge for pressure higher than 10 mbar, shown in figure (3.13(f)).

3.6.2 Internal Temperature Management

After all the external gas management for reducing the pressure to a manageable level for the mass flow controllers, the next step is to systematically cool helium to as low of a temperature as possible by using the two-stage cryocooler. This system of gas lines involves the use of multiple CF16 flanges to allow for removing and breaking the gas lines into multiple pieces to allow for changes without remaking the entire internal system from scratch. Also, we use a combination of 6 mm and 3 mm tubing as well as copper and stainless steel 316 tubing. The internal gas lines can be divided into connections between each stage, i.e.

- Section from vacuum feedthrough to 40-K stage-figure (3.14(a)).
- Section from 40-K stage to 4-K stage-figure (3.14(b)).
- Section from 4-K stage to buffer gas cell-figure (3.14(c)).

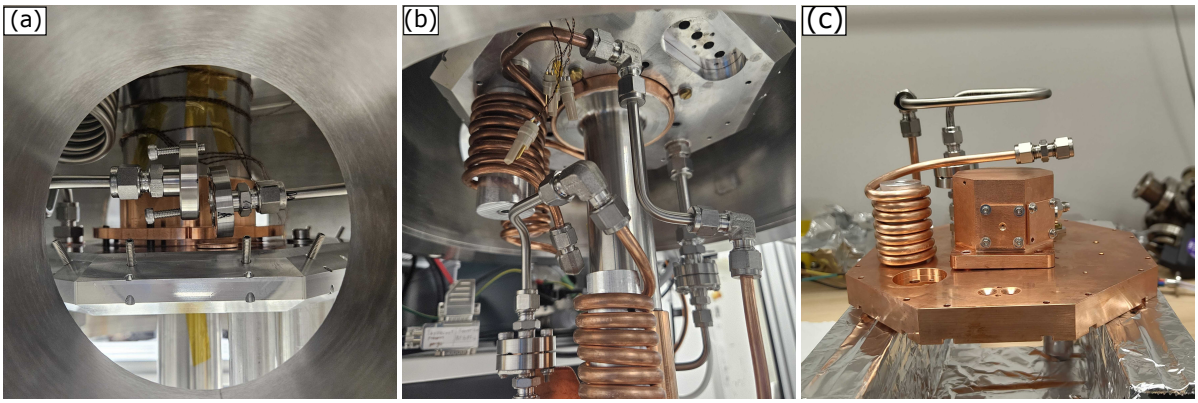

Figure 3.14: (a)Section from vacuum feedthrough to 40-K stage. (b) Section from 40-K stage to 4-K stage. (c) Section from 4-K stage to buffer gas cell.

At each stage, the gas line uses the G1/4-inch threads and converters such that helium flows through the baseplate of the stage, having a better chance of cooling. In both the 40-K and the 4-K stages, a few aluminium columns are also mounted so that we could mount some coils of copper tubing to act as heat exchangers so that they have a better chance of cooling helium down. The copper tubing, while being in contact with the aluminium post, gets cooled down to the temperature of the stage where the column

is mounted. As the helium flows through these cold tubes, it thermalises with them via collisions and lowers the temperature of helium, as shown in figure(3.15(b)). To ensure that there is no thermal shortcut between the two stages, as it will negatively affect the performance of the cryocooler, a stainless steel section is necessary. Thus, the entire gas line fully connected consists of four heat-exchanging coils made out of copper and connecting stainless steel sections, all made using tubing with a 6 mm outer diameter. Only the final section, from the 4-K stage to the buffer gas cell, requires a change in tubing diameter to allow for better flexibility to facilitate easier mounting of the helium feedthrough. With the modular nature of the internal gas lines, we went through lots of iterations to ensure that the tubes were getting close to the temperature of the stages they were connected to. However, only the final iteration is being discussed in this section, as it works for our design goal of cooling helium down to 4 K. However, from previous iterations, we learnt that using thinner internal diameter tubing (3 mm) all throughout the gas lines will not allow the helium to flow through to the buffer gas cell, as the tubes themselves act as a bottleneck and the pressure difference required to maintain a flow is beyond the pressure regime the mass flow controller can operate in. Also, we added stainless steel sections as a buffer to prevent thermal shortcuts. We decided to use stainless steel section of tubing to act as thermal isolation, because when stainless steel was used for all our gas lines, we found that stainless steel is a terrible thermal conductor, especially at sub-100 K temperatures. As even when the cryo has reached its design temperature, the stainless steel section remains 10 K to 20 K above the stage temperature. To see how cool the heat exchangers can get, multiple cool-downs were done while monitoring the temperature at each stage. That was how the final iteration of the gas line was finalised since the temperature in the final heat exchanger was below 4 K, with the fully constructed gas line shown in figures (3.16(a)) and (3.16(b)).

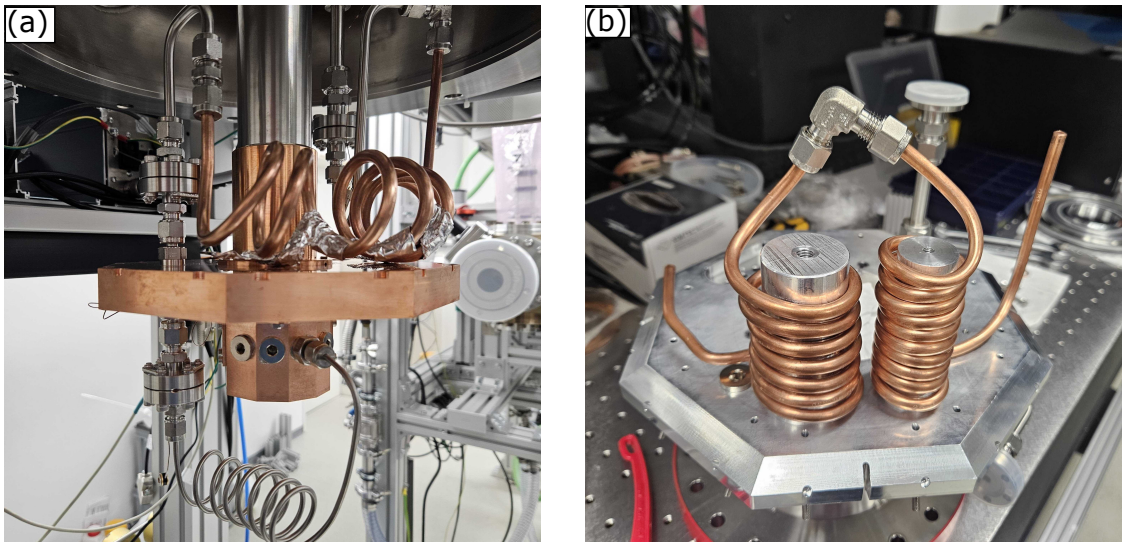

Figure 3.15: (a) Old iteration of heat exchangers. (b) Final iteration of heat exchangers.

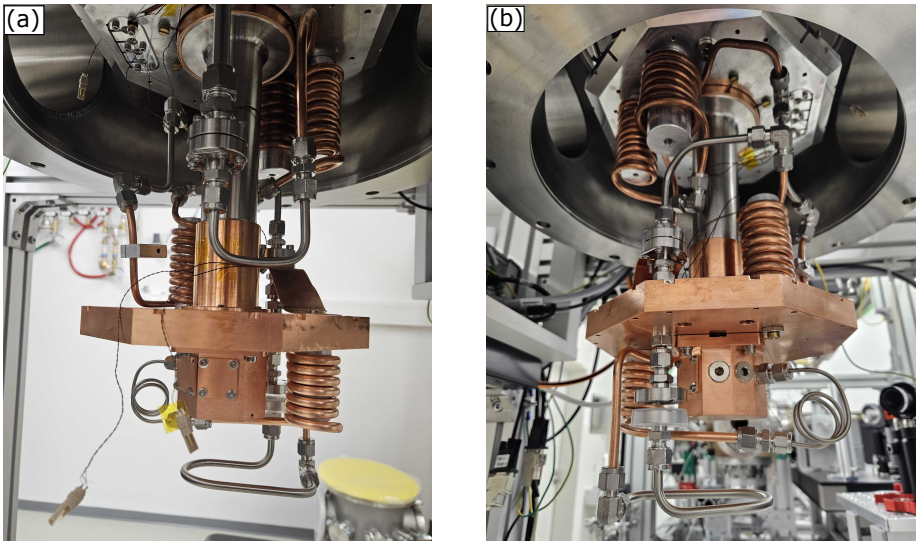

Figure 3.16: (a) and (b) are different views of the fully assembled internal gas line.

3.7 Pre-Vacuum Management System

To ensure that the plethora of turbo pumps that are used in both the source and measurement vacuum chambers have adequate pre-vacuum pressure to work efficiently, enabling fast braking of the turbo pumps as well as future expansion of the entire system, an extensive network of pre-vacuum lines was built. To ensure that we could easily control and isolate each part of the system, multitudes of ball and angle valves were also introduced to this system. We could also monitor the entire system with both analogue and digital vacuum gauges. At the heart of the pre-vacuum system is the 'HiScroll 6' Scroll Pump from Pfeiffer, which is responsible for maintaining the pre-vacuum level throughout these lines. This has a built-in valve that closes automatically during a power loss to ensure that the entire system remains at most 10^{-2} mbar of pressure. The Pre-vacuum management system has three additional roles, while also ensuring adequate vacuum level is maintained for the turbomolecular pumps.

- Braking Turbo Molecular Pumps.
- Connecting to the Helium Recycling System.
- Capturing Excess Sulphur Hexafluoride

The pre-vacuum lines are connected to external nitrogen lines with the help of a needle valve so that parts of the system can be flushed with nitrogen to break the turbo pumps, enabling us to open the chambers quickly. This was essential during the initial parts of the project, as we could easily iterate a change to the system and quickly test its vacuum performance without waiting for the turbo pumps to spool down, which usually take hours. This is also beneficial if we want to flush the vacuum chamber not with ambient air but with nitrogen so that we do not introduce water vapour, especially if we have cold surfaces connected to the cryo and we want these surfaces to warm up faster. Introducing ambient air is not preferable due to the presence of water vapour, which will condense on the colder surfaces. The entire building is connected to a helium recycling system. Therefore, to choose where the exhaust of the scroll pump goes to, either the ambient air of the lab or the helium recycling system, ball valves were

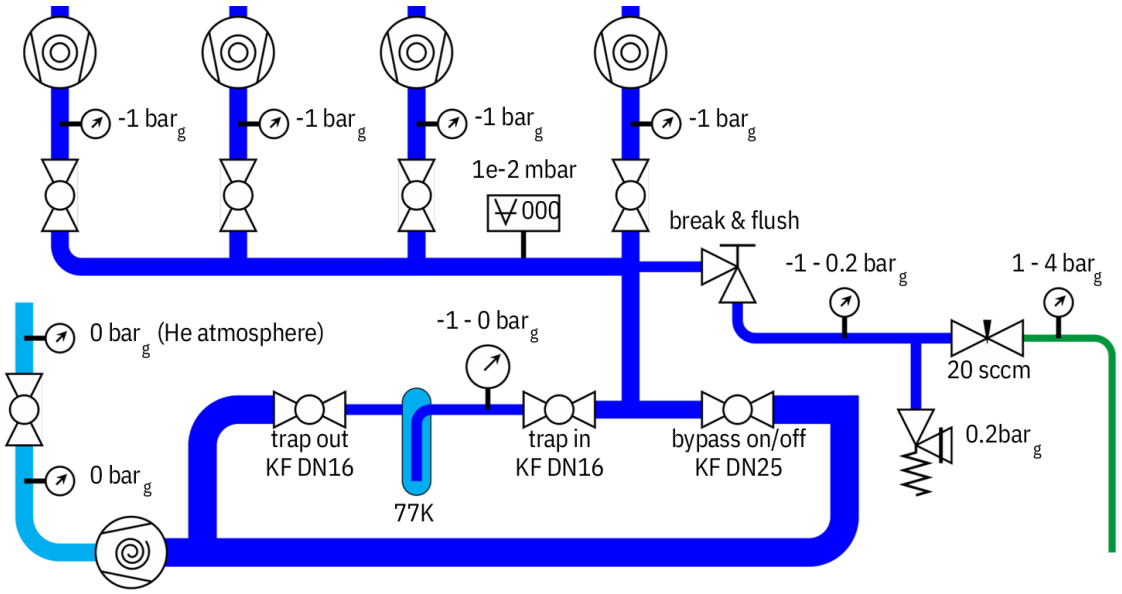

Figure 3.17: Schematic of the pre-vacuum lines: designed by Nick Vogeley.

added to close any one section. As the experiment requires that we actively introduce helium into our system and pump it out, we ensure that most of the helium exhaust goes through the helium recycling line. To finally capture the excess SF_6 that will be used later, we also have built a bypass to allow all the gas from the chambers to go through a glass bottle which will be submerged in liquid nitrogen before being pumped out by the scroll pump. This will liquefy most of the SF_6 so that it can be reused as well. The full pictorial schematic of the pre-vacuum is shown in figure (3.17).

3.8 Data Acquisition

This section gives a brief overview of the data acquisition methods employed to capture data for different parameters like pressure and temperature, as well as the supporting graphical user interface to view said data as well. This helps us keep an eye on the behaviour of the system, which helps us to better understand the limitations of our system. We also employ a data acquisition device to collect data from the photoreceiver to verify our beam parameters as well, which, along with a function generator, can be used to run a simple trigger system to capture data for each ablation pulse.

3.8.1 Temperature and Pressure Monitoring Systems

We use a multitude of digital pressure gauges from Thyracont Vacuum Instruments to monitor the vacuum level of the system in different sections of both chambers. It can be difficult to keep track of these values all the time. Therefore, we use the built-in RS 485 standard Sub-D connections to communicate with all the sensors using a serial-to-Ethernet server to avoid the limitations of signal loss issues of serial-to-USB converters. This allows us to remotely connect to all the sensors using an assigned IP address. Along with the pressure values, we also record temperature readings by again using the serial RS232 communication standard built into the Lakeshore 218 temperature monitoring system. All the

values for these sensors are aggregated into a centralised program with a graphical user interface to easily view all the pressure and temperature values at a glance, getting an idea of where the system is, which will be extremely important while doing measurements. These values are also recorded in a text file as well, with an update frequency of 1 Hz.

3.8.2 Photoreceiver Acquisition Scheme

To detect our fluorescence signal of our ytterbium atoms, we are using a photoreceiver from Laser Components, 'PWPR-2K-SI', which is a silicon PIN photodiode with a built-in amplification circuit, shown in figure (3.18(a)). Since we do not have a continuous source of our target atom/molecule, which is ever present along the helium beam, as it's being produced by an ablation laser, correctly timing the data acquisition is extremely important. For this purpose, we use a function generator to trigger both our ablation laser and the oscilloscope so that we could see the signals from our photoreceiver as well as trigger the data acquisition using a National Instruments 'USB 6003' DAQ device to capture the photoreceiver voltage for a set amount of time after each trigger, as shown in figure(3.18(b)). The ablation laser as well as the built-in counter of the DAQ can be triggered with a Transistor Transistor Logic (TTL) 5V signal. We have set the function generator to produce a square wave with a maximum amplitude of 5V with an extremely low duty cycle of around 0.1% to ensure that both the ablation laser, DAQ and the oscilloscope are triggered by the rising edge of the same short pulse. Along with a small script written to record the active wavelength from the wavelength meter, we can collect data for each shot with an assigned wavelength of probe laser as well.

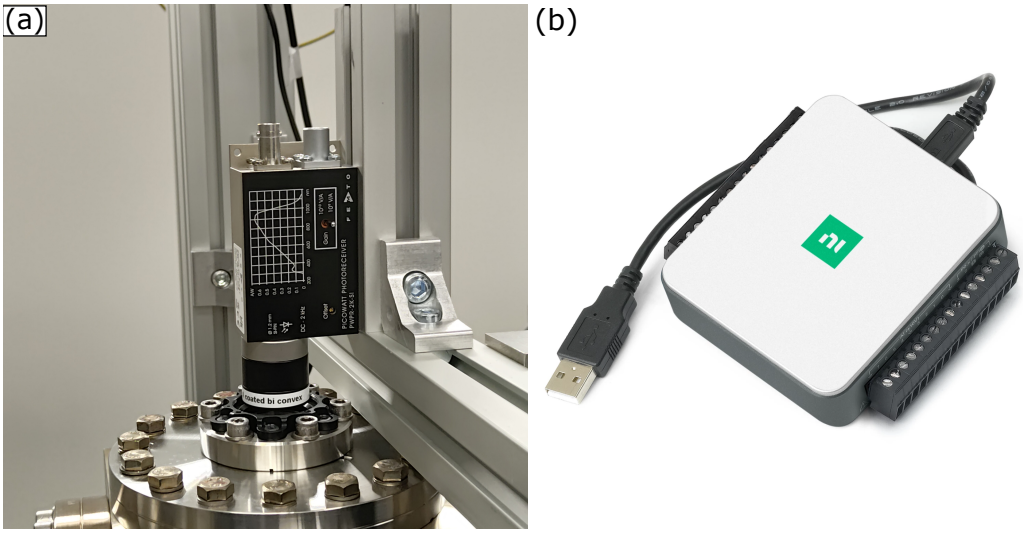

Figure 3.18: (a) Photoreceiver 'PWPR-2K-SI' with built in amplification circuit. (b) Data acquisition system 'USB-6003' from national instruments [16].

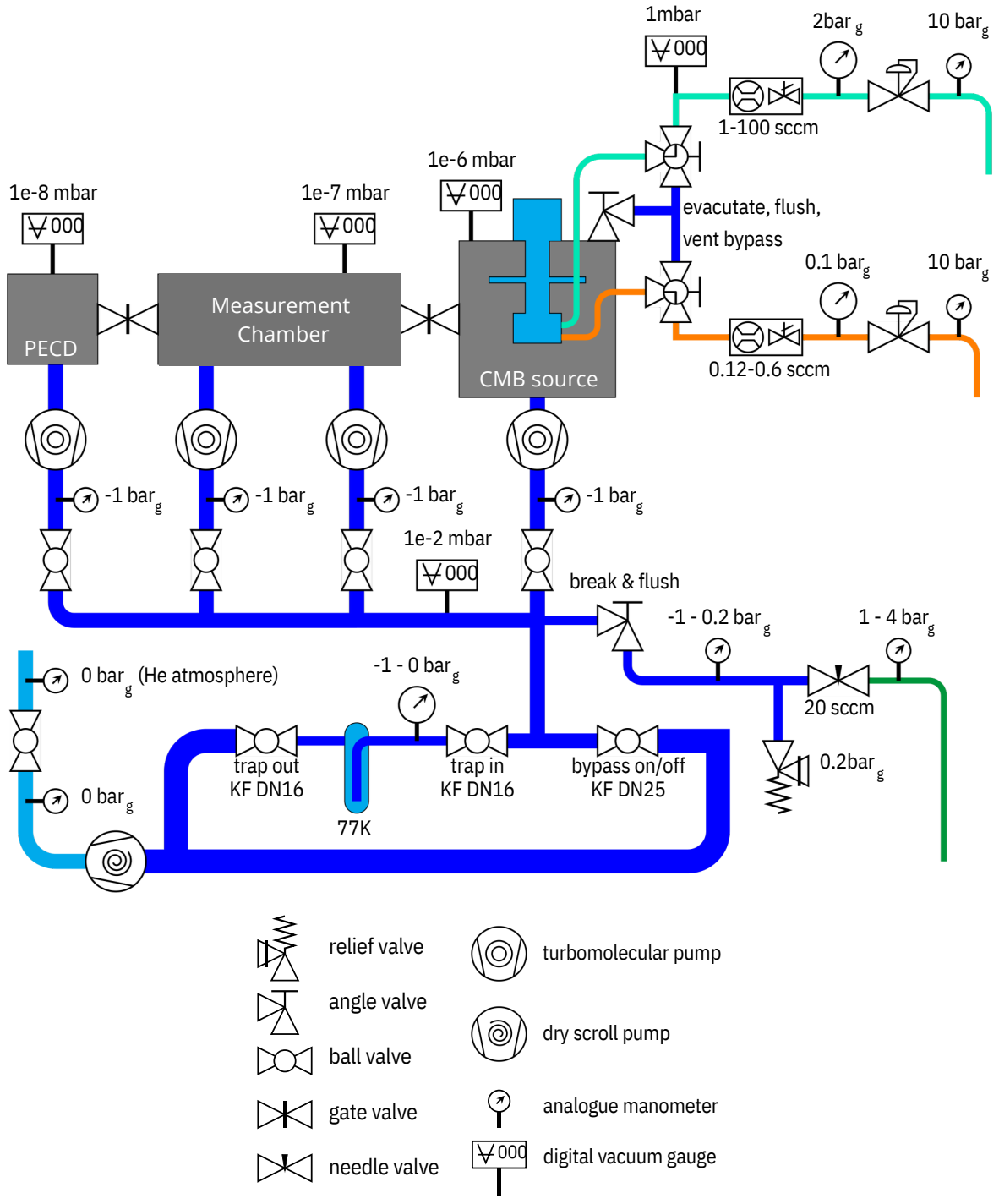

Figure 3.19: Full schematic of the instrument with the source and the measurement chamber along with a proposed PECD chamber for chiral molecules: designed by Nick Vogeley

CHAPTER 4

Characterisation of Cold Beam

To characterise the beam that is produced, we can use two different methods: mass spectroscopy and fluorescence measurements. In mass spectroscopy, we will be using the quadrupole mass spectrometer to detect helium and other gases present inside the vacuum chamber to observe how the levels of these gases change over time with different helium flow rates. This will also be done in conjunction with pressure and temperature sensors to observe how the entire system behaves. With this we can find optimal conditions for the next set of measurements, fluorescence measurements. This will include a typical frequency sweep to identify most of the isotopes of ytterbium, with a two-point measurement to estimate the time of flight and forward velocity of the beam. Finally, a Doppler measurement will also be done to observe the frequency shift and the velocity distributions as well.

4.1 Preliminary Tests

But before we start letting helium into the system, baseline cooling tests were done to better understand how the system works and how low temperatures can be achieved. Therefore, multiple cool-downs were conducted with different increments of radiation shields and gas lines to see if we could hit our desired temperatures on all the critical sections of the system.

The first cool-down was done on the 5th of March 2025 with just the radiation shields and base stages attached to the cryocooler, without any sorption pumps or gas lines. The lowest temperatures hit by the 40-K and the 4-K stages are 31.92 K and 2.69 K, respectively, which gives us a baseline.

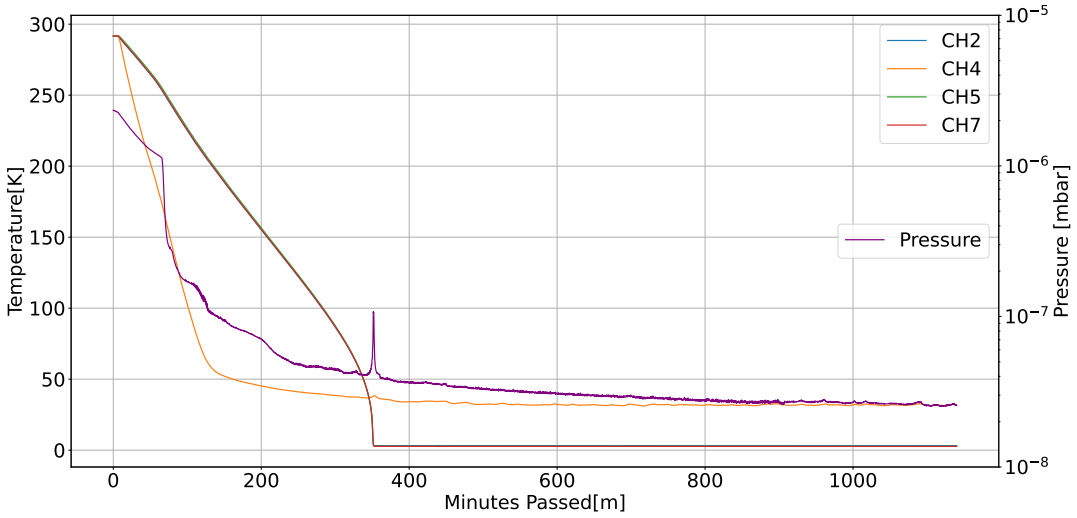

Figure 4.1: A cool-down was conducted on 05-03-2025 with three sensors on the 4-K stage and one on the 40-K stage (channel 4).

Another cool-down was conducted on the 29th of August 2025, this time with the one iteration of gas lines with heat exchangers as shown in figure (4.2(a)). This time, for the cool-down, another temperature sensor was also added to the heat exchangers to monitor its temperature, but it was missing the final heat exchanger. The coil itself reached a temperature of 14.19 K, with the sensor shown in figure (4.2(a)). As mentioned in section (3.4), the measurement table hosts the quadrupole mass spectrometer (QMS). After reaching base temperature, helium was let into the system, and background mass spectroscopy was done using the QMS to see the composition of the background vacuum. After that, helium was let into the system at different flow rates to see its effect, which is plotted in figure (4.2(b)).

It is evident from the QMS background measurement that the helium levels oscillate in the chamber, which also causes pressure fluctuations as well. A detailed analysis will be done using the above-mentioned heat exchanger layout as well as the 4 heat exchanger layouts.

4.2 Mass Spectroscopy

With the QMS it is difficult to observe ytterbium, as it is only introduced into the beam whenever there is an ablation however; the helium beam is continuous. Therefore, the QMS can be used to observe and characterise the helium beam. Together with helium levels, the temperature and pressure of both chambers were also monitored as well. We come back to the measurement done on 29th of August 2025. We plot the pressure of the source chamber with the readings from the QMS on helium level within the measurement chamber, together with the temperature of the cell. We observe that all the oscillations occur almost simultaneously.

From the above plots, it is quite evident that the environment inside the chamber is not stable, as when helium is introduced into the chamber, the charcoal sorption pumps start absorbing the excess helium, though their capacity is quite limited. When the charcoal pumps cannot absorb any more helium and are overwhelmed, the walls of the 4-K enclosure start to heat up, which cascades to decreasing sorption capacity, leading to more helium not absorbed by the sorption pumps, until the temperature of

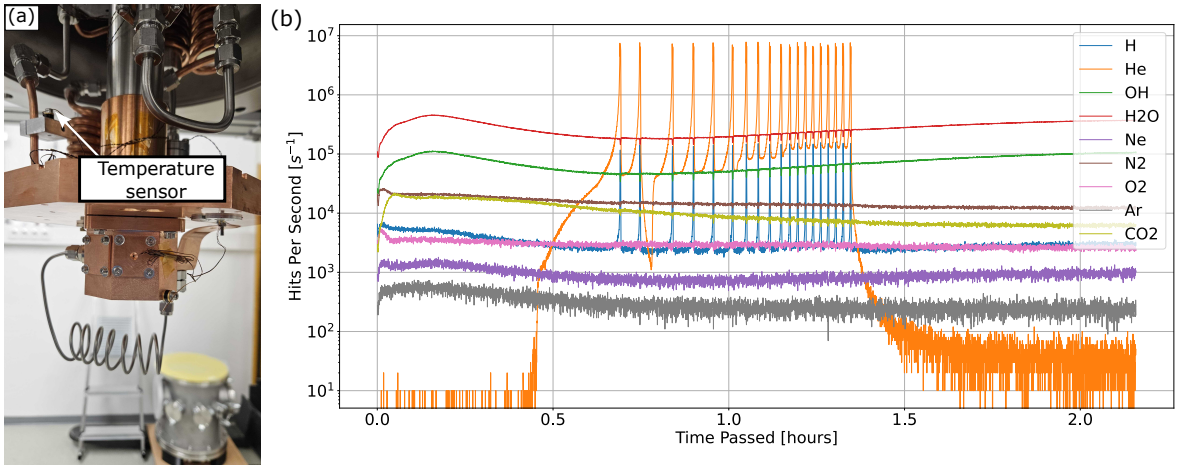

Figure 4.2: (a) 3 heat exchanger format of the helium gas line (b) Background measurement of the QMS with varying flow rates of helium done on 29-08-2025.

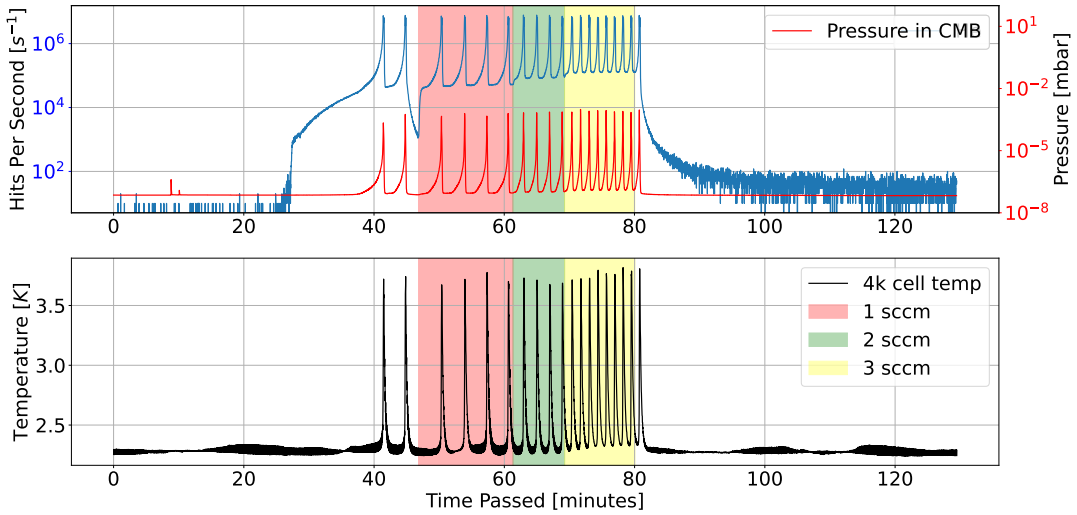

Figure 4.3: The helium test was done on 29-08-2025 with three heat exchanger setups as shown in figure (4.2(a)). Different flow rate regimes of the helium are plotted as shaded regions after the charcoal pumps have been saturated.

the walls and sorption pump rises high enough to release all the excess helium into the chamber, causing a pressure spike up to 10^{-3} mbar. At such high pressures, the beam that is produced will get dispersed by random collisions as the mean free path of both ytterbium and helium becomes really low. Therefore, a low-pressure environment is necessary to ensure that the beam remains undisturbed. We postulated that one of the reasons we are seeing these fluctuations may be because the helium itself is not cooled down to low temperatures. Therefore, another heat exchanger was also added, as shown in the figure (4.4(c)).

We again did another cool-down on 4th of September 2025, while recording the temperatures of both the sorption pumps directly (figure (4.4(a))) and the fourth heat exchanger (figure (4.4(b))), and

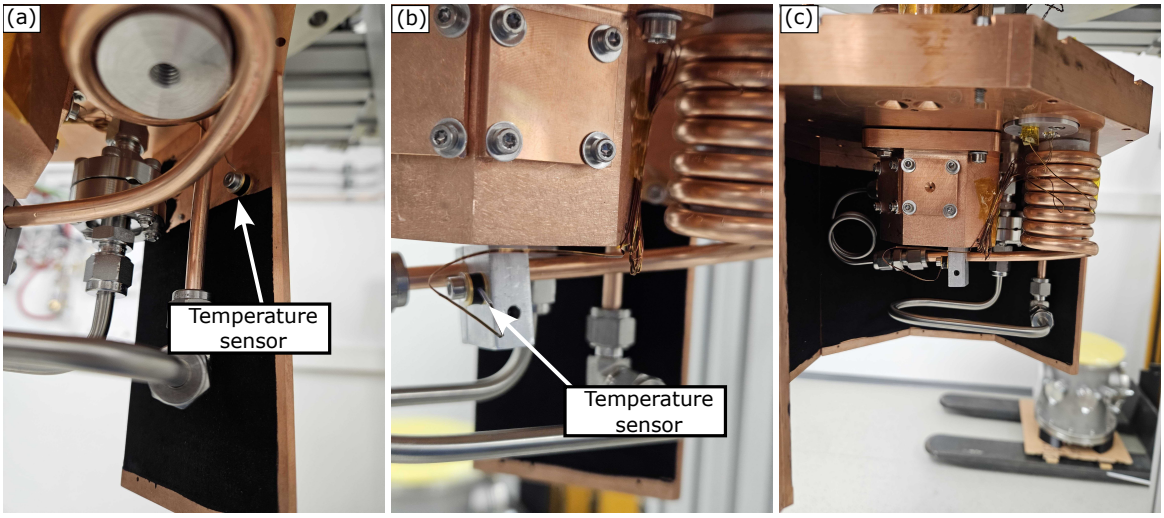

Figure 4.4: (a) A temperature sensor mounted on the wall of the 4-K shield to record the temperature of the sorption pumps. (b) A temperature sensor mounted on the end of the final heat exchanger for helium (c) The fourth heat exchanger for the helium added inside the 4-K enclosure.

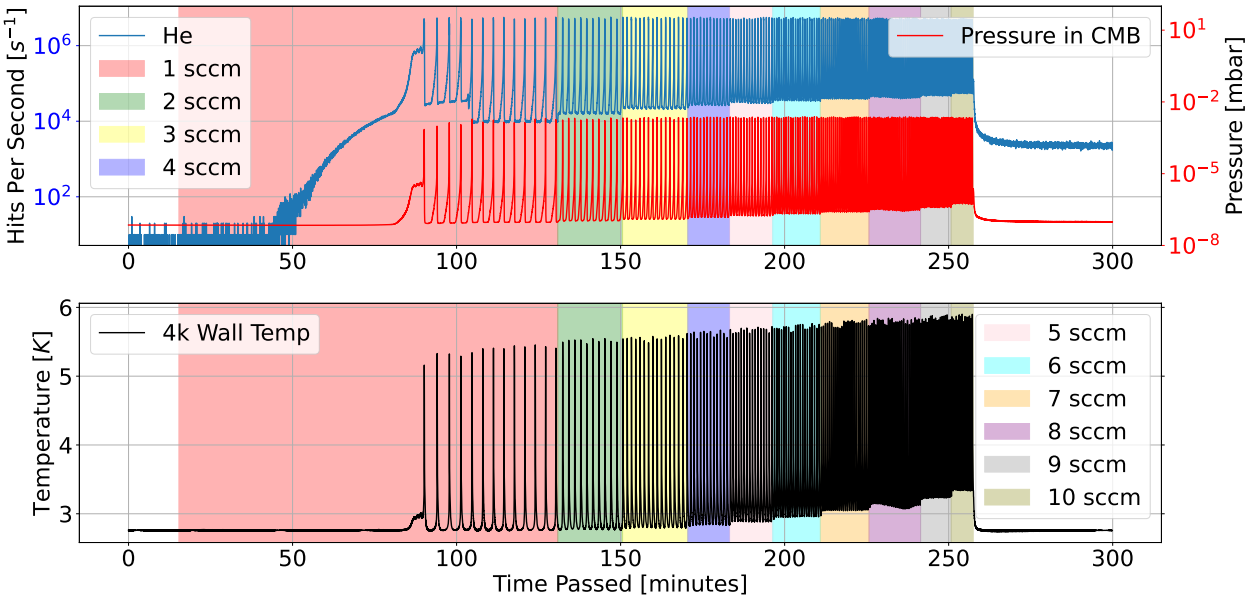

Figure 4.5: The helium test was done on 04-09-2025 with the four heat exchanger setups as shown in figure (4.4(c)). Different flow rate regimes of the helium are plotted as shaded regions after the charcoal pumps have been saturated.

we observed that the temperature of the heat exchanger was 2.75 K after the cool-down, which should be enough to cool helium. Another test was conducted to observe the helium levels in the chamber at different flow rates. Unfortunately we still observe the oscillation even with sub-4 K cooled helium, as

shown in figure (4.5).

When helium is first being introduced into the chamber, it requires a time delay of about 30 minutes before helium is detected by the QMS, as the majority of it is being absorbed by the sorption pump, and that is the most suitable background pressure regime to perform measurements, as the vacuum level in the source chamber remains below 10^{-6} mbar, implying that the pressure in the measurement chamber remains below 10^{-7} mbar, as shown in figure (4.6). To take repeated measurements, the charcoal sorption pumps have to be regenerated, which means that the excess helium has to be removed from them. Which will happen naturally due to excess helium or can be done manually by turning the cryocooler off so that the 4-K stage warms up above 8 K, releasing all the helium, which will eventually be pumped out by the turbo pumps. After which the cryocooler can be turned on again, cooling the system down for more measurements.

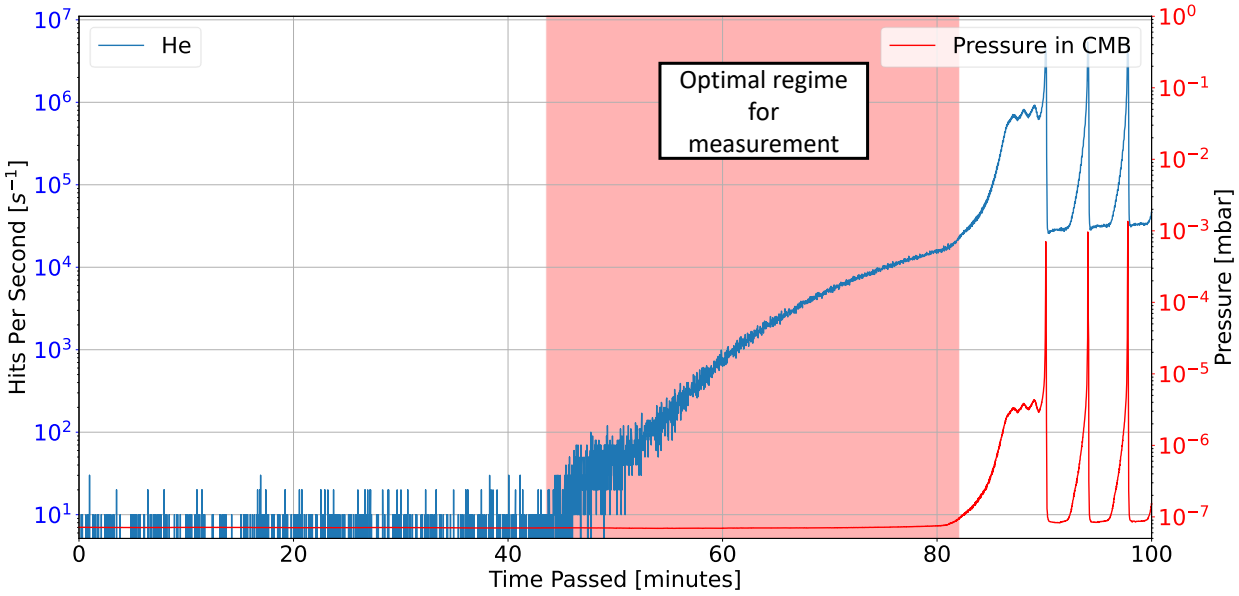

Figure 4.6: Optimal conditions to conduct fluorescence measurements.

4.3 Fluorescence Measurements

Since it is clear when the pressure levels are stable after helium flow is started, we can move on to fluorescence measurements. However, before any measurements can be taken, the effects of the ablation laser has to be explored. Since the production of ytterbium atoms involves the use of a high-power ablation laser, we would like to observe how the power of the ablation laser causes the 4-K stage to heat up. The power of an ablation laser can be controlled by changing the voltage from the main controller to the laser head. In the table (4.1), baseline temperature changes to different operating voltages are recorded. However, it is important to note that the power of the ablation laser varies drastically by

changing the pulse frequency and also decreases as the frequency decreases. As even at the peak power of the ablation laser the temperature of the cell still remains below 4 K, we can take some fluorescence measurements without being concerned about the temperatures. Because the laser will not be run at its maximum frequency, the cell will cool down between shots, and overall less energy will be transferred to the cell.

Table 4.1: Tabular representation of the voltage to power relationship for the ablation laser.

Voltage(V)	**Energy per pulse (mJ) @ 10Hz**	**Cell temperature (K)**	**Wall temperature (K)**
–	–	2.70	2.48
490	24	3.03	2.77
500	31	3.15	2.90
510	40	3.29	3.07
520	49	3.44	3.17
530	60	3.53	3.34
540	72	3.64	3.46
550	82	3.74	3.57
560	90	3.87	3.70
570	100	3.95	3.78

4.3.1 Time of Flight measurement

To estimate the forward velocity of the Yb beam, a two-point measurement was done. In both positions, a 399 nm probe laser, tuned to a frequency of roughly 751.52624 THz, was pointed perpendicular to the Yb beam with a photoreceiver pointed down onto the beam to detect any fluorescence signals, as shown in figure (4.7). With the trigger scheme mentioned in section (3.8.2), we can do triggered measurements with the photoreceiver and do a time-of-flight measurement between the two positions.

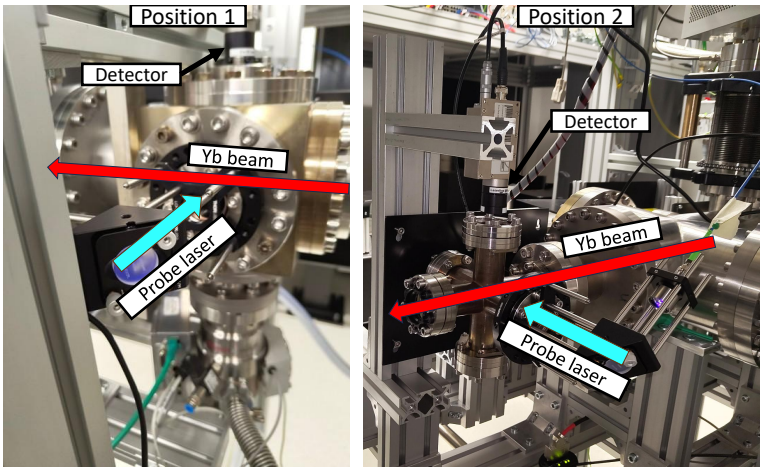

Figure 4.7: Positions 1 and 2 for the doppler free measurement.

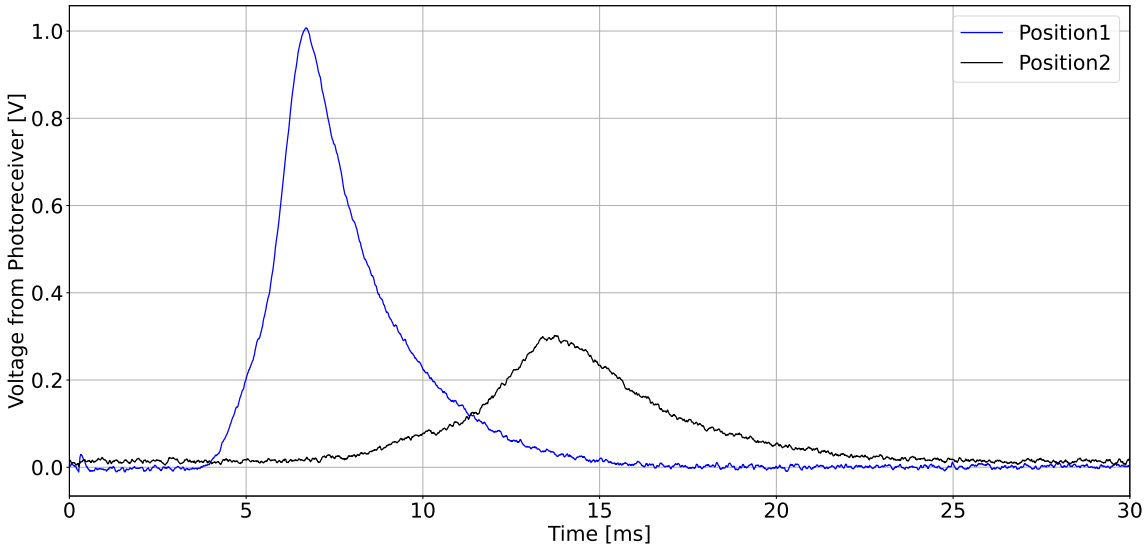

Figure 4.8: Brightest photoreceiver signals from position 1 in dark blue and position 2 in black.

By taking the two brightest signals from the multitude of ablation shots that were performed and recorded at both positions as plotted in figure (4.8), we can estimate the time step recorded by the DAQ where half of the atoms has passed through a measurement point by taking a weighted median on the intensity plot in figure (4.8). If w_i is the voltage measured by the photoreceiver after the trigger, the median time step satisfies the condition:

$$t_{\text{median}} = t_k := \left\{ \frac{\sum_{i=1}^{k-1} w_i}{\sum_{i=1}^{n} w_i} \leq \frac{1}{2} \right\} \quad \text{and} \quad \left\{ \frac{\sum_{i=k+1}^{n} w_i}{\sum_{i=1}^{n} w_i} \leq \frac{1}{2} \right\} \tag{4.1}$$

Thus, the two time steps where half the atoms have crossed the detector are $t_{\text{median}}(\text{Pos.1}) = 7.34$ ms and $t_{\text{median}}(\text{Pos.2}) = 14.34$ ms. Thus, the time of flight is $\Delta t = (7.00 \pm 0.01)$ ms. The distance between the two detection positions is 82 cm, thus giving a forward velocity of the beam of $v = (117.14 \pm 0.02)$ m/s.

However, when we start to ablate at a single point, the material starts to get removed from the ablation spot, changing the spot distance from the lens. This causes the spot to move away from the focal plane of the lens, leading to decreased concentration of energy and less ytterbium being ablated. This is also visible if we plot consecutive ablation events. We can observe a decrease in the brightness or intensity of fluorescence signals recorded by the photoreceiver as shown in figure (4.9). Therefore, it is essential to keep changing the ablation spot to maintain a comparable brightness. It was evident that the typical lifetime of an ablation spot is around 20 shots before the signal dies out. After all the measurements were taken for this thesis, the target of ytterbium was taken out, and the damage is shown in the figure (4.10).

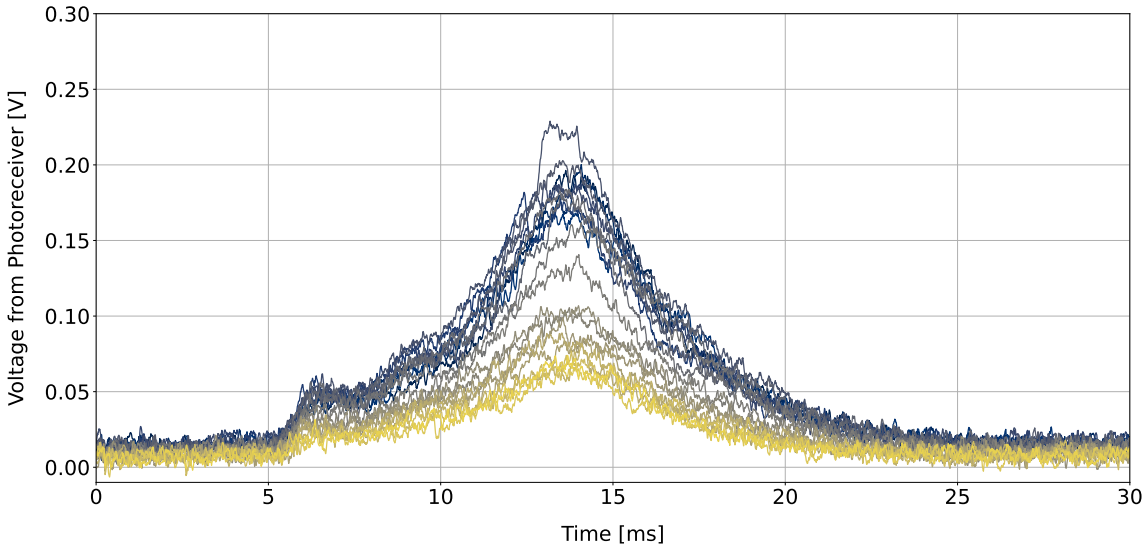

Figure 4.9: Photoreceiver signal for 20 consecutive ablation shots. The first shot is coloured dark grey, and the twentieth shot is represented by the colour yellow.

Figure 4.10: Ytterbium target after all the measurements were taken, with roughly three thousand shots.

4.3.2 Isotopes of Ytterbium

A simple frequency sweep across a 2 GHz range is to be performed to detect most of the prominent isotopes of ytterbium, along with their hyperfine splitting. However, because of the limited lifetime of the

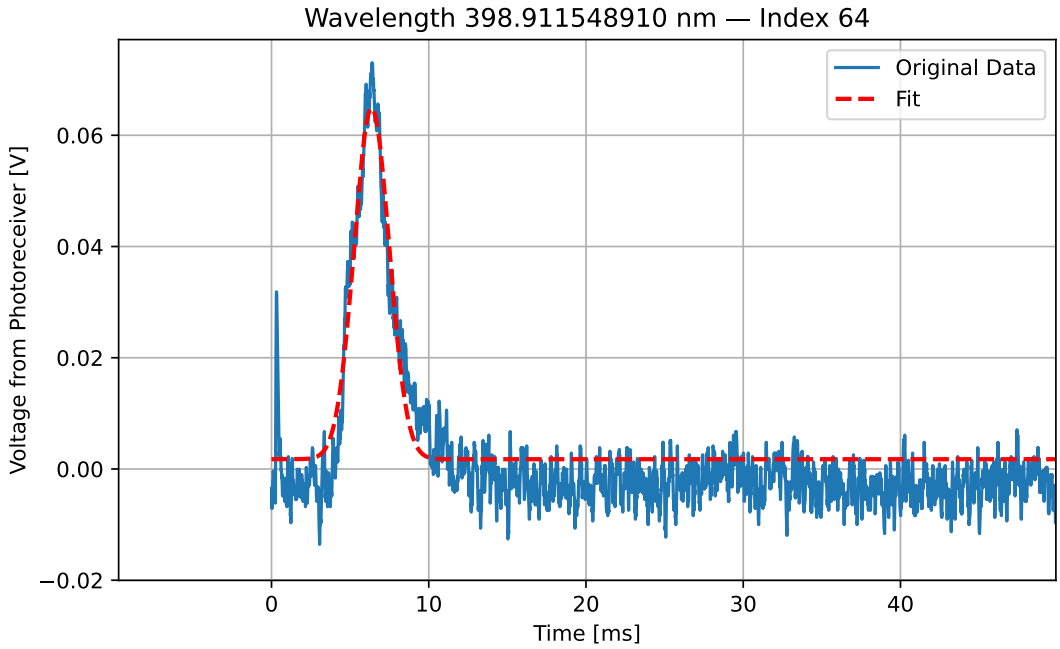

Figure 4.11: An example of a Gaussian fit with equation (4.2) was performed to each shot of all data sets to estimate the maximum brightness of each shot.

ablation spot, a full frequency sweep across 2 GHz is not possible, and it had to be done in sets. Because of this, it is difficult to also compare the brightness levels between sets, as even if a fresh ablation spot is chosen, the pressure and temperature conditions may be different, changing the brightness of each shot.

To estimate the brightness of each shot, a Gaussian function with a constant factor was fitted to each ablation shot; that is,

$$V(t) = Ae^{-\frac{(t-t_0)^2}{2\sigma^2}} + C \tag{4.2}$$

was fitted to each shot to take into account the noise present in each signal, with an example shown in figure (4.11). After that, all the maximum brightness for each ablation shot was calculated at t_0, i.e., $V(t)_{\max} = A + C$, and saved with its wavelength values. Then all data sets were plotted with a frequency detuning with the reference being ${}^{174}f_0 = 751.526246$ THz which is estimated from a Gaussian fit to the Doppler-free measurement of the ^{174}Yb isotope, similar to the discussion in section (4.4). All eleven sets of measurements are plotted in figure (4.12). By adding the typical isotopes' transition from the ${}^1S_0$ subshell to the ${}^1P_0$ subshell with different hyperfine levels of the excited state, obtained from the literature [17], we can observe that they match well, and we see most of the prominent isotopes of ytterbium as well.

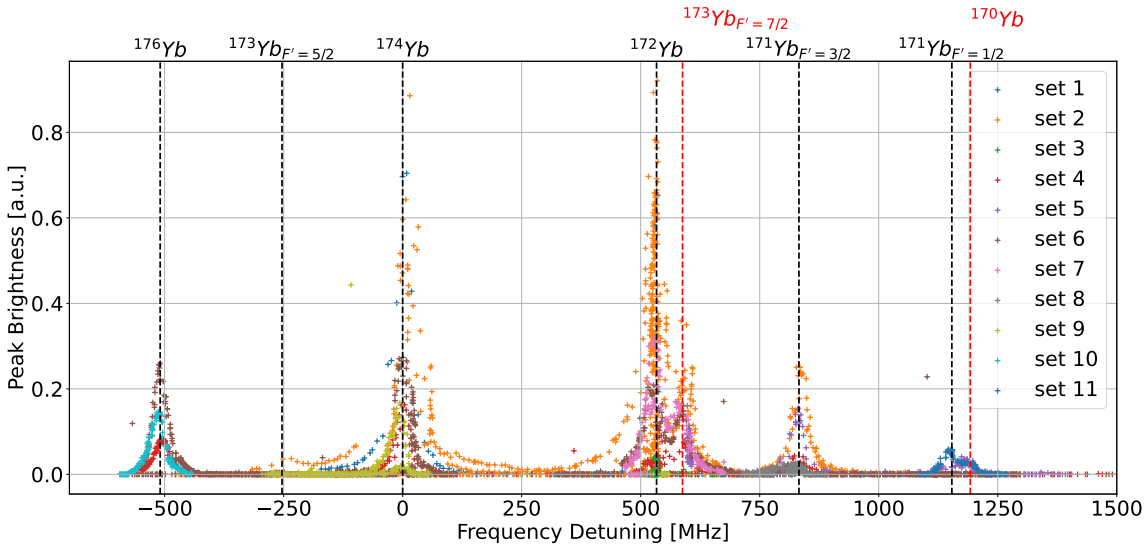

Figure 4.12: Frequency sweep for all major ytterbium isotopes with all the typical frequency detuning with respect to the transition of ^{174}Yb, marked on the top axis, obtained from [17].

4.4 Velocity Distribution Analysis

For calculating the velocity distribution of our beam, a Doppler measurement is required. A counter-propagating probe beam is steered towards the ytterbium beam, and by placing the detector on top of the atomic beam, we can detect the Doppler shift of a particular isotope of ytterbium, with the setup shown in figure (4.13).

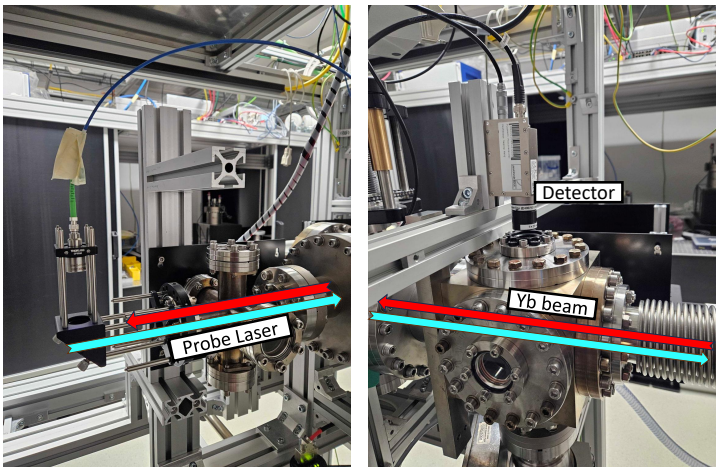

Figure 4.13: Setup for detecting Doppler shifted peaks of different isotopes.

Before we continue, let us first choose our reference. As observed in figure (4.12), it is quite easy to identify an isotope's transition by referencing to literature and their shape. For the purpose of velocity distribution, we will choose the ^{172}Yb transition from the $^1S_0$ subshell to the $^1P_0$ subshell. Therefore, we

will be fitting a Gaussian to one particular set of frequency sweeps to estimate a transition frequency with respect to our wavelength meter. The function to be fitted is equation (4.3) with μ being the transition frequency.

$$P(f) = Ae^{-\frac{(f-\mu)^2}{2\sigma^2}} + C \tag{4.3}$$

Because of the close proximity of the ^{172}Yb isotope transition to the $^{173}\mathrm{Yb}_{\mathrm{F'=7/2}}$ transition, only half of the data set belonging to the ^{172}Yb isotope's transition was used, as shown in figure (4.14).

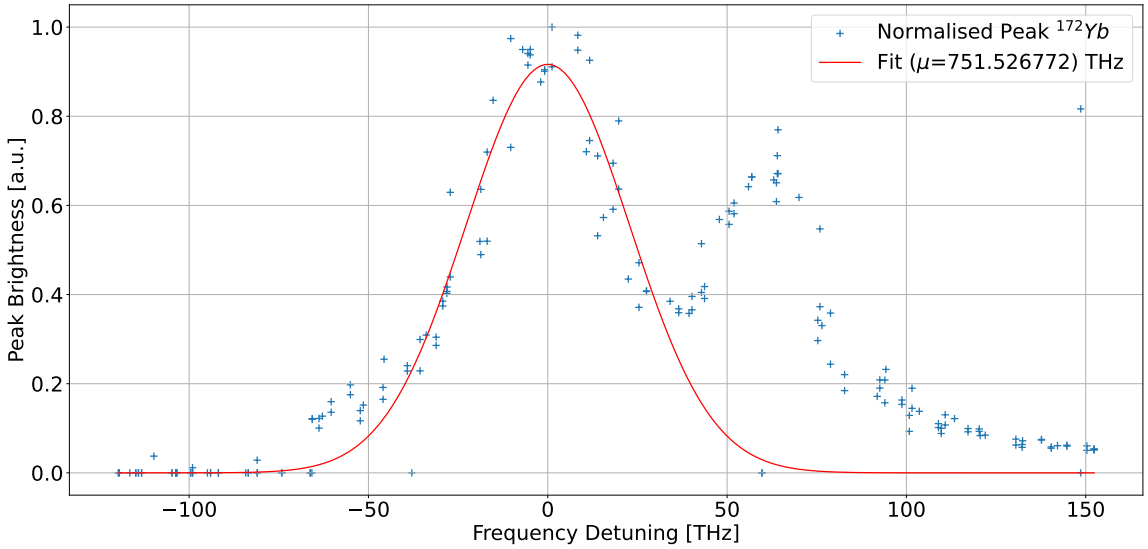

Figure 4.14: Doppler-free frequency scan with detuning estimated with the fit parameter of the Gaussian fit for the ^{172}Yb transition.

With the Gaussian fit we estimate the transition frequency of the ^{172}Yb isotope from the $^1S_0$ subshell to the $^1P_0$ subshell to be $\mu = f_0 = 751.526772$ THz with a standard deviation of $\sigma = 22$ MHz. As the beam is moving towards the source, the transition frequency of the atom in its rest frame will increase (blue shift), so calculating the frequency shift for a forward velocity of roughly 117 m/s results in roughly 293 MHz red shift to hit resonance. Therefore, by scanning in this region for the ^{172}Yb isotope's red shift with a forward velocity of 117 m/s, we see the frequency sweep as shown in the figure (4.15).

Because of the limited lifetime of an ablation spot, a new spot had to be found for concurrent measurements, leading to varying brightness levels. Therefore, major portions of the data set had to be excluded to fit a Gaussian function to this frequency shift. This results in a frequency shift for the transition of the ^{172}Yb isotope to $\mu = f_1 = 751.526439$ THz with a standard deviation of $\sigma = 68$ MHz. If we assume that the broadening of the Doppler-shifted distribution is entirely due to thermal broadening, we can estimate the temperature of our beam using the relation for Doppler broadening in equation (4.4)[18].

$$T = \frac{m}{k_B}\left(\frac{\sigma c}{f_0}\right)^2 \tag{4.4}$$

With m being the mass of the ^{172}Yb isotope, k_B the Boltzmann constant, σ the standard deviation for the

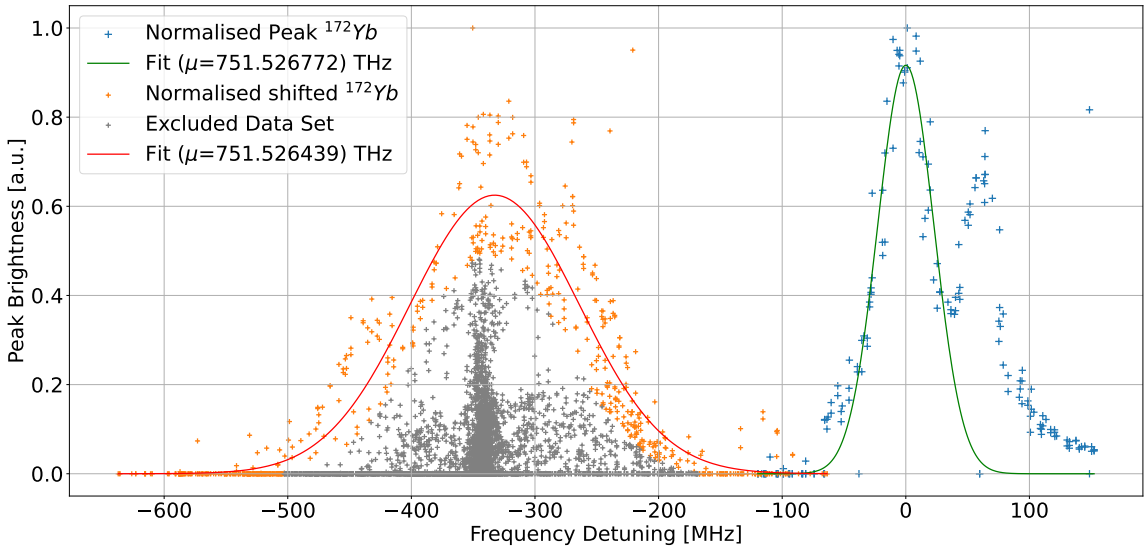

Figure 4.15: Doppler-shifted frequency scan with detuning estimated from ^{172}Yb Doppler-free transition.

Doppler-shifted peak, and f_0 the Doppler-free transition frequency. Since all the above parameters are known, we can estimate the beam temperature as $T = (15.4 \pm 0.5)$ K. Also, using the non-relativistic approximation for Doppler shift, we can also estimate the average velocity of the forward beam using the relation

$$v_{\text{mean}} = c\frac{f_0 - f_1}{f_0} \tag{4.5}$$

which gives us a mean forward velocity of $v_{\text{mean}} = (132 \pm 9)$ m/s.

Using the equation (4.5), a velocity distribution can also be calculated to effectively understand the flow regime the beam is operating in. By using the Doppler-free transition f_0 and calculating the velocity of the data points that were used for the Gaussian fit from figure (4.15), we can plot a velocity distribution as shown in figure (4.16). With a close look, it looks like the velocity distribution profile is what you would expect for a buffer gas cell, that the distribution is in a partially hydrodynamic regime. Therefore, as the partially hydrodynamic regime is closer to the supersonic regime, we will fit a supersonic velocity distribution approximation to our data and estimate the forward velocity and temperature of our beam. The function to be fitted is

$$p_{\text{sup}}(v) = Av^3 \exp\left(\frac{M(v - v_0)^2}{2k_B T_{\text{beam}}}\right) \tag{4.6}$$

and the fit result is shown in figure (4.16). The mass of the target species is represented by M, which is $M = 172$ u. The forward velocity of the beam from the fit is $v_0 = (112.4 \pm 0.7)$ m/s, and the beam temperature from the fit is $T_{\text{beam}} = (18.0 \pm 0.6)$ K.

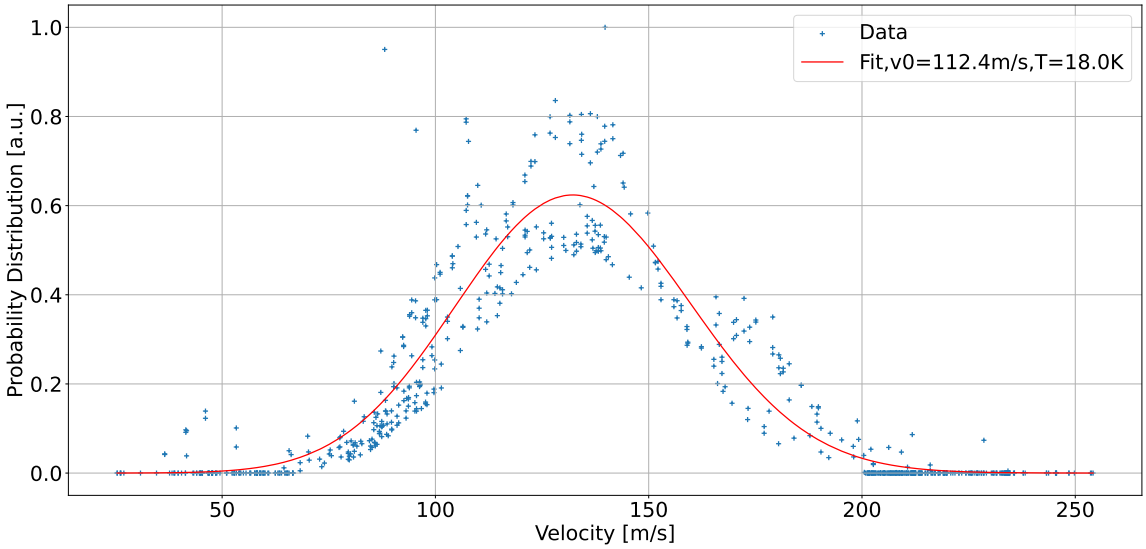

Figure 4.16: The supersonic flow regime approximation to velocity distribution of the beam.

CHAPTER 5

Conclusion

The goal of this thesis was to produce a cold molecule beam, and that has been demonstrated with the help of ytterbium. There are many possible improvements that can be made to the machine to make it much more stable. However, the goal of producing a beam has been achieved. With minimal iterations, mainly to the gas lines, we could effectively add another gas such as sulphur hexafluoride to react to the ytterbium metal produced by ablation and form ytterbium mono-fluorides, which is one of the candidates with a fairly approachable Frank-Condon factor allowing this candidate to be laser cooled and trapped. Even if laser cooling and trapping is not the goal, we have a general machine which can cool down multitudes of not just simple atoms and diatomic molecules but also much more complex chiral molecules as well. This can be achieved by directly introducing the complex molecule into the cell via a hot injection method, ensuring that the line connecting to the cell, through which the molecules are introduced, doesn't get blocked due to freezing. With this we are capable of producing a cold beam of any target, as long as it can be introduced into the cell as a vapour. But before we end, let us aggregate all the beam characteristics.

5.1 Beam Characteristics

The forward velocity of the beam calculated from the two-point measurement from the fluorescence of the beam as calculated in section (4.3.1) is 117 m/s. The velocity estimation from the supersonic beam approximation, as done in section (4.4), is 112 m/s, which matches with the time of flight measurement. There is a small discrepancy between the two measurements, and one can argue that the counter-propagating light used for the Doppler measurement will most likely also slow the beam down, or partially the atoms that are in resonance with the red detuned light. While we are actively sweeping across the frequency, it is evident that there will be some effect of laser slowing on the atoms that are on resonance. Another reason for the forward velocity difference could be that the external pressure conditions in the chamber might be different. As the pressure outside the cell is different, the expansion of helium, which is highly dependent on the pressure difference between the cell and the surrounding pressure outside the orifice of the cell, will also be different. And as we have seen this behaviour in the figure (4.5), even when the system is not oscillating to high pressure values, it does keep changing while helium is being introduced into the system. There could also be no feasible shot-to-shot comparison, as we have also seen in figure (4.10) how repeated shots of ablation cause the target to get out of the focal

plane for the ablation laser to effectively transmit its energy to the cell, introducing different amounts of ytterbium in the cell and shifting the overall brightness of the fluorescence measurements.

We also estimated the beam temperature to be roughly 15 K from the Doppler-spread measurements, and with velocity distribution, the temperature was measured to be roughly 18 K, much higher than the cell and the helium temperatures that were recorded, which were below 4 K. We have also seen that the typical forward velocity is also a bit slow as compared to expected results from buffer gas sources, shown in figure (2.4). We can argue that, because of the inherent limitation of the machine in its current state, it's not feasible to operate the system at high flow rates of helium, which may have resulted in fewer collisions between the buffer gas and the ytterbium atoms, causing the atoms to not fully thermalise with the buffer gas and the cell itself.

5.2 Possible Improvements

One of the main problems or bottlenecks for running the instrument is mainly the changing pressure of both the source chamber and the measurement chamber, as it quite often keeps oscillating even after repeated warm-ups and cool-downs of the cryocooler. Therefore, one of the most obvious improvements would be to maintain the pressure in both chambers as low as possible, which could be done via larger turbomolecular pumps. However, a better solution would be to use more surface area for charcoal sorption pumps, as, while effective, these are clearly being overwhelmed by even a relatively small flow rate of helium. To do so, we could either redesign the 4-K radiation shield for a larger surface area or use a better grade of coconut charcoal with a larger grain size so that there is even more surface that is exposed to helium and not covered by the epoxy that holds the charcoal to the radiation shield itself. Another improvement could be to increase the pressure difference between the source chamber and the measurement chamber by either adding another turbo pump to the section connecting the two chambers or using a smaller connection between the chambers to increase the pressure difference. Finally, we could also employ some skimmers to remove excess helium out of the beam but still leave the beam relatively unperturbed to reduce the helium entering the measurement chamber. Lastly, another improvement that is required would be a better ytterbium target, as even after all the previous improvements, the lifetime of an ablation target will remain limited. So, either a larger ytterbium target or a rotatable target will be required so that there is always a fresh spot for ablation, and maybe we could also include a 4f system of lenses to manually change the focal plane of the final lens mounted on the cell itself.

5.3 Future Outlook

After showing the capability of producing a cold beam using ytterbium atoms, the future steps for the current machine will be to implement some, if not all, of the improvements discussed in the previous section and finally, use the machine to produce a cold molecule beam of chiral molecules, particularly fenchone, and conduct some Photoelectron Circular Dichroism (PECD) measurements on it. Along with this development, another source machine will also be developed to produce calcium mono-fluoride to laser slow and trap these molecules first in a magneto-optical trap. And later, the molecules will be loaded onto a tweezer array, with the goal of producing a programmable array of qubits for quantum simulations.

CHAPTER 6

Appendix

Probe Laser for Ytterbium Detection

The 399 nm laser required for probing the ytterbium signals comes from a tunable diode laser from 'Toptica Photonics'. The laser sits in a different room, which is why it is fibre-coupled to a 25 m long single-mode fibre so that it can be moved to the lab where the experiment sits. This is also where the wavelength meter is placed so that the laser and wavelength meter can be placed together and the frequency of the dye laser can be tuned remotely.

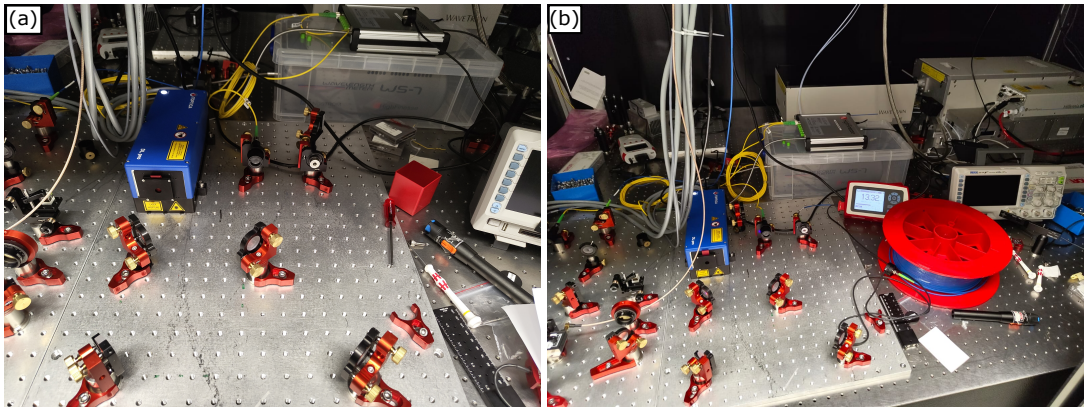

Figure 6.1: (a) Optical Setup for the 399 nm tunable diode laser for fibre-coupling, and a beam sampler for wavelength measurement. (b) Fibre coupling to 25 m fibre for transport to the experiment.

Oven for Ytterbium

Before we finalised the method of producing the atoms inside the buffer gas cell, the idea of producing a continuous beam of ytterbium using an oven was floated. However, due to the difference in temperature between the cold buffer gas cell and the hot oven, there were quite a few challenges to be solved before this could be implemented. The main issue is how to isolate the hot oven and the cold buffer gas cell, as

the power required for producing hot ytterbium atom vapour will be much more than the capacity of the 4-K stage of the cryocooler. Also, there were no good candidates for insulating materials for the oven that were also vacuum stable. While there are some plastics that are vacuum stable, they cannot handle the extreme temperature required for vaporising ytterbium. Finally, the ceramic glue required for producing the oven in the first place was also not stable in a vacuum, producing flakes, and would most likely contaminate the vacuum environment. For all the above-mentioned reasons, it was decided not to use the hot oven and instead we decided to deploy the tested method of using laser ablation.

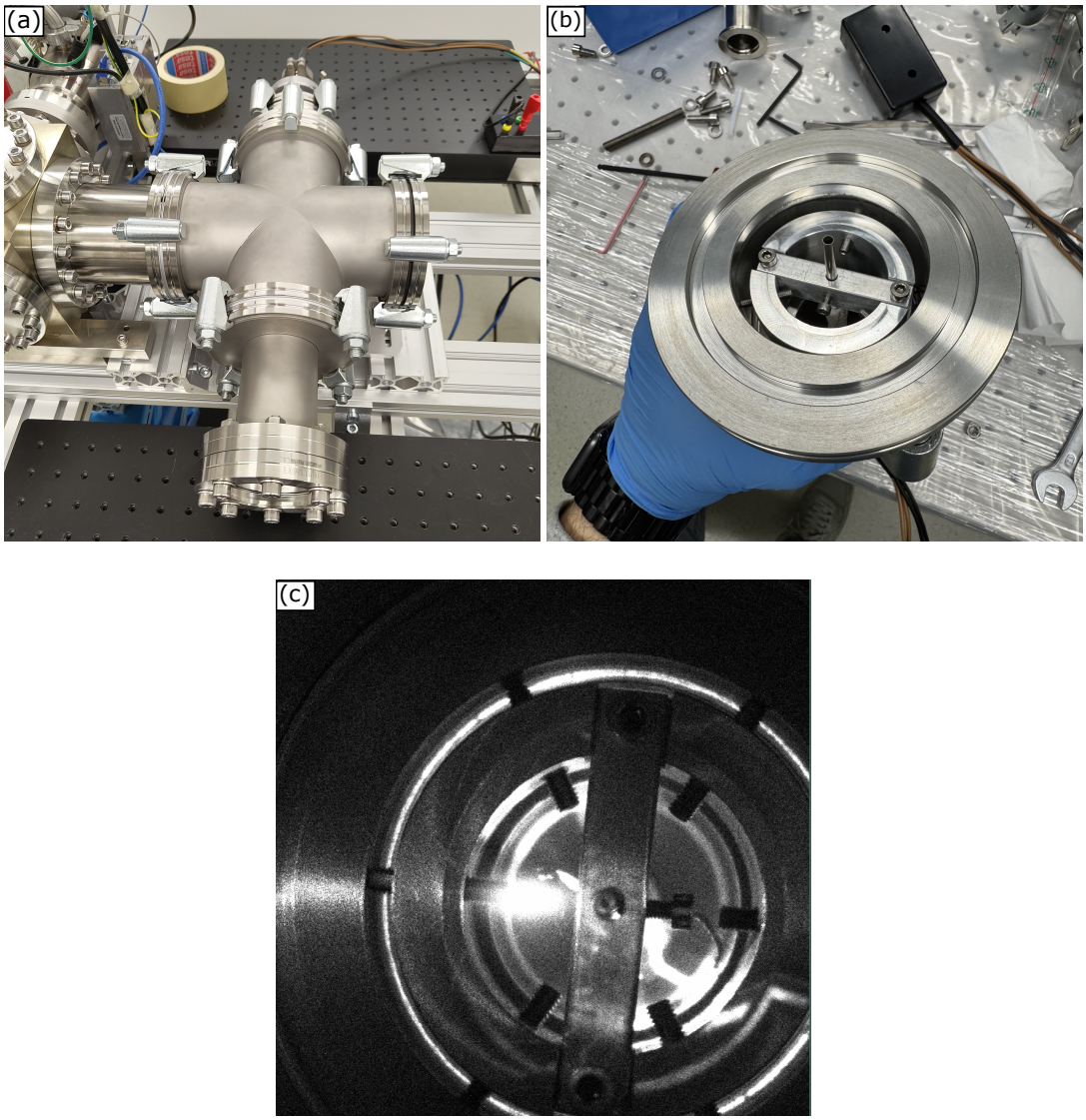

Figure 6.2: (a) Chamber used for testing the oven.(b) Oven holder that will be mounted to the chamber (c) Ytterbium beam fluorescence, recorded with a camera.

Before the idea of using an oven for the production of a continuous beam was fully scrapped, the oven

itself was mounted inside a small vacuum chamber with multiple windows to do some fluorescence measurements. A 2 GHz frequency sweep was done, and the maximum brightness for different frequencies was recorded and plotted in figure (6.3).

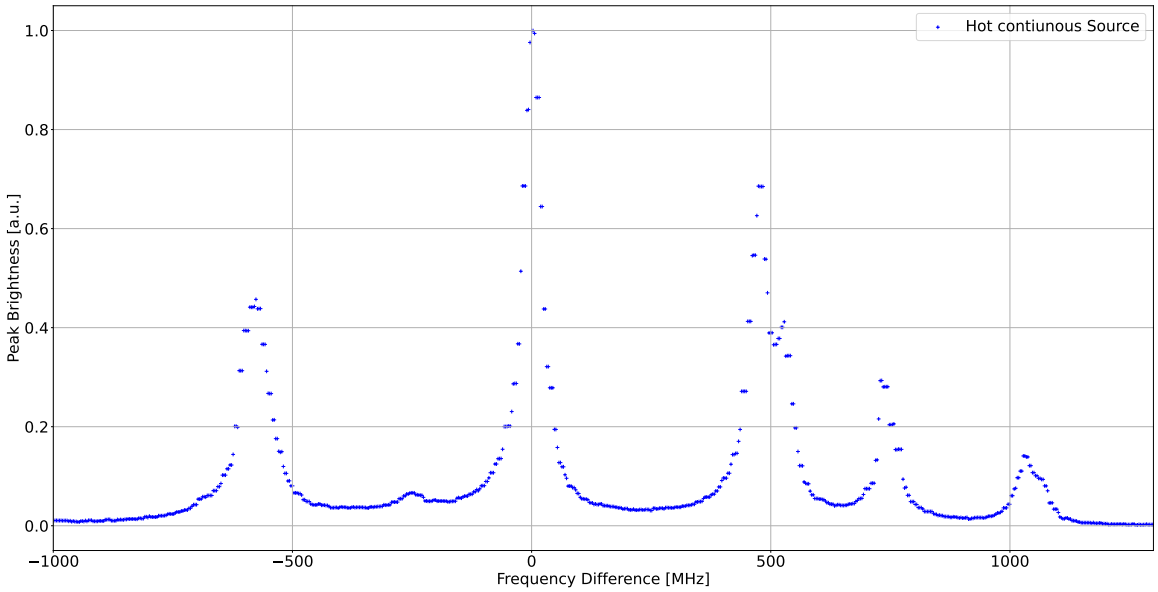

Figure 6.3: Frequency sweep for ytterbium isotopes with the frequency reference being the transition of the ^{174}Yb isotope.

Detection of Ytterbium using QMS

Before the optical setup to detect ytterbium was built, we tried to detect ytterbium using the QMS. But because of the nature of the ytterbium beam, produced by ablation, it made it very difficult to detect any isotope of ytterbium. Many tests were run with the QMS and the ablation laser, but none of them were fruitful. After which we wanted to explore the idea of doing triggered measurements; however, due to time constraints as well as previous experience with the oven for optical measurements, it was decided to directly move on to optical fluorescence measurements.

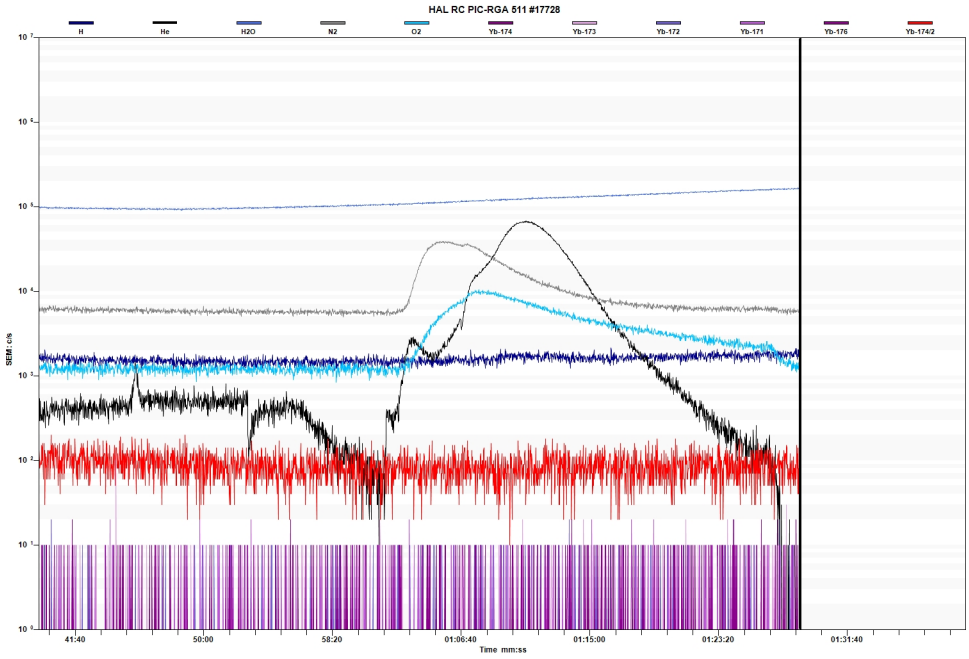

Figure 6.4: One of the many failed QMS test done to detect any isotope of Yb.

Doppler-free Fit of ^{174}Yb isotope

To set the frequency reference for the plot in figure (4.12), the Doppler-free fit was done to one of the sets of frequency sweeps done. And this results in the $^{174}f_0$ = 751.526246 THz with a standard deviation of σ = 17 MHz. The fit is shown in figure (6.5).

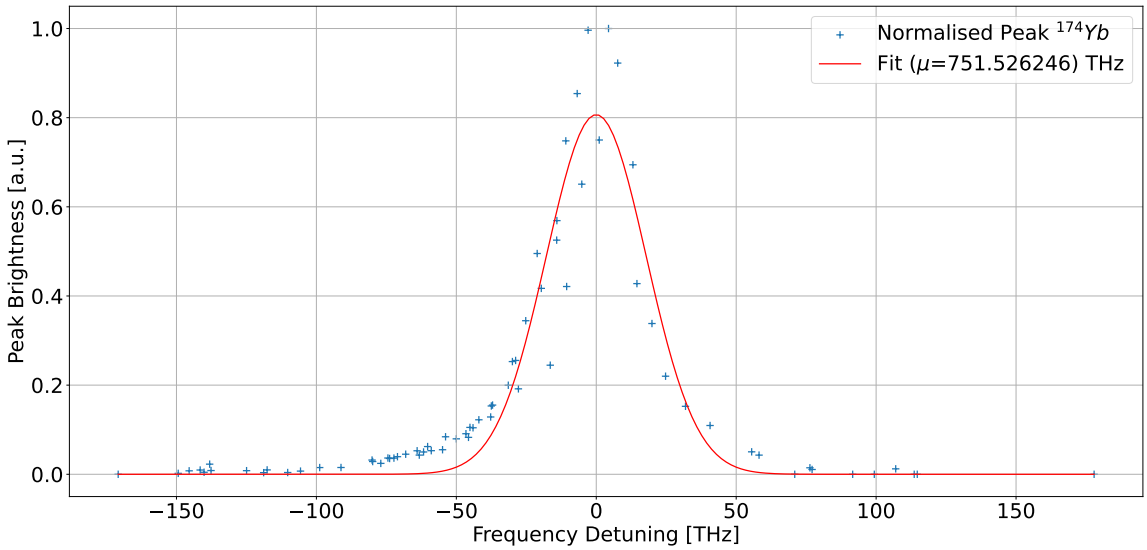

Figure 6.5: Doppler-free frequency scan with detuning estimated with the fit parameter of Gaussian fit for the^{174}Yb transition.

List of Figures

Bibliography

[1] M.S. Safronova et al. “Search for new physics with atoms and molecules”. In: *Rev. Mod. Phys.* 90.2 (29th June 2018). Publisher: American Physical Society, p. 025008. DOI: 10.1103/RevModPhys.90.025008. URL: https://link.aps.org/doi/10.1103/RevModPhys.90.025008 (visited on 24/11/2025).

[2] Kang-Kuen Ni, Till Rosenband and David D. Grimes. “Dipolar exchange quantum logic gate with polar molecules”. In: *Chem. Sci.* 9.33 (22nd Aug. 2018). Publisher: The Royal Society of Chemistry, pp. 6830–6838. ISSN: 2041-6539. DOI: 10.1039/C8SC02355G. URL: https://pubs.rsc.org/en/content/articlelanding/2018/sc/c8sc02355g (visited on 24/11/2025).

[3] Mark Brouard, David H. Parker and Sebastiaan Y. T. van de Meerakker. “Taming molecular collisions using electric and magnetic fields”. In: *Chem. Soc. Rev.* 43.21 (6th Oct. 2014). Publisher: The Royal Society of Chemistry, pp. 7279–7294. ISSN: 1460-4744. DOI: 10.1039/C4CS00150H. URL: https://pubs.rsc.org/en/content/articlelanding/2014/cs/c4cs00150h (visited on 24/11/2025).

[4] Maarten C Mooij et al. “A method to determine the phase-space distribution of a pulsed molecular beam”. In: *Journal of Physics B: Atomic, Molecular and Optical Physics* 58.1 (2024), p. 015303. DOI: 10.1088/1361-6455/ad9a2e. URL: https://doi.org/10.1088/1361-6455/ad9a2e.

[5] S. E. Maxwell et al. “High-Flux Beam Source for Cold, Slow Atoms or Molecules”. In: *Phys. Rev. Lett.* 95 (17 2005), p. 173201. DOI: 10.1103/PhysRevLett.95.173201. URL: https://link.aps.org/doi/10.1103/PhysRevLett.95.173201.

[6] David Patterson and John M. Doyle. “Bright, guided molecular beam with hydrodynamic enhancement”. In: *The Journal of Chemical Physics* 126.15 (Apr. 2007), p. 154307. ISSN: 0021-9606. DOI: 10.1063/1.2717178. eprint: https://pubs.aip.org/aip/jcp/article-pdf/doi/10.1063/1.2717178/14858917/154307_1_online.pdf. URL: https://doi.org/10.1063/1.2717178.

[7] Nick Vogeley, Bernd Bauerhenne and Daqing Wang. *Hydrodynamic Effects in Cryogenic Buffer Gas Cells: Design Insights from Hybrid Simulations*. 6th Aug. 2025. DOI: 10.48550/arXiv.2508.04364. arXiv: 2508.04364[quant-ph]. URL: http://arxiv.org/abs/2508.04364 (visited on 17/10/2025).

[8] M. R. Tarbutt. "Laser cooling of molecules". In: *Contemporary Physics* 59.4 (2nd Oct. 2018). Publisher: Taylor & Francis _eprint: https://doi.org/10.1080/00107514.2018.1576338, pp. 356–376. ISSN: 0010-7514. DOI: 10.1080/00107514.2018.1576338. URL: https://doi.org/10.1080/00107514.2018.1576338 (visited on 17/10/2025).

[9] N. J. Fitch and M. R. Tarbutt. "Laser cooled molecules". In: vol. 70. 2021, pp. 157–262. DOI: 10.1016/bs.aamop.2021.04.003. arXiv: 2103.00968[physics]. URL: http://arxiv.org/abs/2103.00968 (visited on 17/10/2025).

[10] K. Walzer et al. "Comparison of organic thin films deposited by supersonic molecular-beam epitaxy and organic molecular-beam epitaxy: The case of titanyl phthalocyanine". In: *Surface Science* 600.10 (May 2006), pp. 2064–2069. ISSN: 00396028. DOI: 10.1016/j.susc.2006.02.039. URL: https://linkinghub.elsevier.com/retrieve/pii/S0039602806002226 (visited on 22/11/2025).

[11] Nicholas R. Hutzler, Hsin-I Lu and John M. Doyle. "The Buffer Gas Beam: An Intense, Cold, and Slow Source for Atoms and Molecules". In: *Chem. Rev.* 112.9 (12th Sept. 2012). Publisher: American Chemical Society, pp. 4803–4827. ISSN: 0009-2665. DOI: 10.1021/cr200362u. URL: https://doi.org/10.1021/cr200362u (visited on 10/11/2025).

[12] A. D. White et al. "Slow molecular beams from a cryogenic buffer gas source". In: *Phys. Rev. Res.* 6 (4 2024), p. 043232. DOI: 10.1103/PhysRevResearch.6.043232. URL: https://link.aps.org/doi/10.1103/PhysRevResearch.6.043232.

[13] Sumitomo Heavy Industries. *RDE-418D4 4K Cryocooler Series*. https://shicryogenics.com/product/rde-418d4-4k-cryocooler-series/. [Online; accessed 20 November 2025]. 2025.

[14] Lakeshore cryotonics. *Model 218 cryogenic temperature monitor*. https://www.lakeshore.com/products/categories/overview/temperature-products/cryogenic-temperature-monitors/model-218-temperature-monitor. [Online; accessed 20 November 2025]. 2025.

[15] Thyracont Vacuum Industries. *VSM Vacuum Transducer*. https://thyracont-vacuum.com/en/product/vsm7xd-smartline-pirani/. [Online; accessed 20 November 2025]. 2025.

[16] National Instruments. *USB-6003*. https://www.ni.com/nl-nl/shop/model/usb-6003.html. [Online; accessed 20 November 2025]. 2025.

[17] Dipankar Das et al. "Absolute frequency measurements in Yb with 0.08 ppb uncertainty: Isotope shifts and hyperfine structure in the 399nm $^1S_0 \rightarrow ^1 P_0$ line". In: *Phys. Rev. A* 72.3 (23rd Sept. 2005). Publisher: American Physical Society, p. 032506. DOI: 10.1103/PhysRevA.72.032506. URL: https://link.aps.org/doi/10.1103/PhysRevA.72.032506 (visited on 23/11/2025).

[18] Livio Gianfrani. "Linking the thermodynamic temperature to an optical frequency: recent advances in Doppler broadening thermometry". In: *Philosophical Transactions of the Royal Society A: Mathematical, Physical and Engineering Sciences* 374.2064 (28th Mar. 2016). Publisher: Royal Society, p. 20150047. DOI: 10.1098/rsta.2015.0047. URL: https://royalsocietypublishing.org/doi/10.1098/rsta.2015.0047 (visited on 24/11/2025).